



저작자표시-비영리-변경금지 2.0 대한민국

이용자는 아래의 조건을 따르는 경우에 한하여 자유롭게

- 이 저작물을 복제, 배포, 전송, 전시, 공연 및 방송할 수 있습니다.

다음과 같은 조건을 따라야 합니다:



저작자표시. 귀하는 원저작자를 표시하여야 합니다.



비영리. 귀하는 이 저작물을 영리 목적으로 이용할 수 없습니다.



변경금지. 귀하는 이 저작물을 개작, 변형 또는 가공할 수 없습니다.

- 귀하는, 이 저작물의 재이용이나 배포의 경우, 이 저작물에 적용된 이용허락조건을 명확하게 나타내어야 합니다.
- 저작권자로부터 별도의 허가를 받으면 이러한 조건들은 적용되지 않습니다.

저작권법에 따른 이용자의 권리는 위의 내용에 의하여 영향을 받지 않습니다.

이것은 [이용허락규약\(Legal Code\)](#)을 이해하기 쉽게 요약한 것입니다.

[Disclaimer](#)

공학박사 학위논문

Multilayer Epitaxial Growth of
Organic Molecules for Efficient Small
Molecular Organic Solar Cells

유기분자의 다층 에피택시 성장을 통한 고효율
단분자 유기태양전지

2015년 2월

서울대학교 대학원

재료공학부 하이브리드재료 전공

김 태 민

Multilayer Epitaxial Growth of Organic Molecules for Efficient Small Molecular Organic Solar Cells

지도 교수 김 장 주

이 논문을 공학박사 학위논문으로 제출함
2015년 2월

서울대학교 대학원
재료공학부 하이브리드재료 전공
김 태 민

김태민의 공학박사 학위논문을 인준함
2015년 2월

위 원 장 조 원 호 (인)

부위원장 김 장 주 (인)

위 원 서 용 석 (인)

위 원 홍 종 인 (인)

위 원 김 효 정 (인)

Abstract

Multilayer Epitaxial Growth of Organic Molecules for Efficient Small Molecular Organic Solar Cells

Kim Tae-Min

Department of Materials Science and Engineering

The Graduate School

Seoul National University

Organic photovoltaic cells (OPVs) have been attracted in last decades due to their large area applicable, low-cost, non-toxicity and flexibility advantages. Unfortunately, OPVs have relatively low power conversion efficiency (η_p) compared to inorganic based photovoltaic devices. Moreover, the stability of the OPVs are too poor to use for the power generation. Thus, improvement of η_p and the stability are key issues for the manufacturing of the OPVs. In this thesis, the use of templating materials for improving the optoelectronic properties of the organic layers are reported and the mechanism of the templating effects is discussed.

Firstly, we report that the use of molybdenum oxide (MoO_3) and copper iodide (CuI) as a double interfacial layer improves the η_p and the photostability at the same time in zinc phthalocyanine (ZnPc) based photovoltaic cells. The absorption of the ZnPc film is enhanced 1.6 times by insertion of

CuI as a template layer. Resultantly, the OPV with a CuI interfacial layer increases the efficiency significantly to 3.3%. However, the photo-stability is lowered even further. The time-of-flight secondary ion mass spectrometry (TOF-SIMS) analysis reveals that the diffusion of Cu atoms or ions is the origin of the photo-degradation of the device. Insertion of the MoO₃ layer between the indium tin oxide (ITO) and CuI prevents the diffusion of Cu atoms or ions under UV illumination.

To reveal the origin of the templating effects, the optoelectronic properties of lead-phthalocyanine (PbPc) and the performance of OPVs have been investigated by using three copper halogen compounds (CuCl, CuBr, CuI) possessing different lattice parameters as the templating layers. The crystallinity of the PbPc films was the highest on CuI followed by CuBr and CuCl, resulting in the broadening of Q-band absorption in the same order. The templating effects were able to be described by heteroepitaxial growth of organic molecules on the templating layers and the dimensionless potential calculated using a lattice model for the overlayer-substrate systems showed good correlation between the degree of epitaxy and the crystallinity of PbPc overlayers. Furthermore, the performance of OPVs was consistent with the prediction from the calculation results and the observation from the optical and structural analyses.

Finally, the templating effect extends to multilayers to increase the crystallinity and to modify the orientation of the crystals of PbPc and C₇₀ layers at the same time by adopting CuBr as a new templating layer on ITO.

The formation of a monoclinic phase with a preferred orientation of (320) for PbPc and a fcc phase with a preferred orientation of (220) for C₇₀ on the PbPc layer is revealed by X-ray diffraction (XRD) patterns. The multilayer epitaxy results in an increase of the exciton diffusion lengths from 5.6 to 8.8 nm for PbPc and from 6.9 to 13.8 nm for C₇₀ to enhance the η_p of the planar heterojunction OPVs composed of PbPc and C₇₀. The heteroepitaxy model also explains the multilayer epitaxy.

Keywords: organic photovoltaic, small molecule, vacuum processing, crystal growth, organic epitaxy, photo-stability

Student Number: 2011 - 30784

Contents

Abstract	i
Contents.....	ii
List of Tables	vi
List of Figures	vii
Chapter 1 Introduction	1
1.1 Motivation and outline of thesis.....	1
1.1.1 Motivation	1
1.1.2 Outline of thesis.....	3
1.2 Organic photovoltaic cells.....	6
1.2.1 Working principles of organic photovoltaic cells.....	6
1.2.2 Basic characterization of organic photovoltaic cells	8
1.2.3 Vacuum deposited small molecular organic photovoltaic cells	14
1.3 Epitaxial growth of organic molecules and simple lattice modelling.....	23
1.3.1 Epitaxial growth of organic molecules.....	23
1.3.2 Energetic consideration and simple lattice modelling.....	27
Chapter 2 High efficiency and high photo-stability zinc- phthalocyanine based planar heterojunction solar cells with a double interfacial layer	33

2.1	Introduction	33
2.2	Experimental.....	36
2.2.1	Device fabrication and characterization	36
2.2.2	Device aging condition.....	37
2.2.3	Depth profiling	37
2.3	Result and discussion.....	38
2.3.1	Current density-voltage characteristics	38
2.3.2	Photo-stability of devices	40
2.3.3	Depth profiling by using Time-of-Flight-Secondary Ion Mass Spectroscopy	45
2.4	Conclusion.....	51
Chapter 3 The epitaxial growth of lead phthalocyanine on copper halogen compounds as the origin of templating effects		
52		
3.1	Introduction	52
3.2	Experimental	54
3.2.1	Device fabrication and characterization	54
3.2.2	Characterization of thin films.....	55
3.3	Result and discussion	56
3.3.1	Optical and structural analyses of lead phthalocyanine films on various copper halogen compounds layer.....	56

3.3.2 Lattice modelling by energetic consideration.....	59
3.3.3 Investigation of surface morphology.....	64
3.3.4 Photovoltaic characteristics of devices.....	64
3.4 Conclusion.....	69
Chapter 4 Multilayer epitaxial growth of lead phthalocyanine and C₇₀ using CuBr as a templating layer for enhancing the efficiency of organic photovoltaic cell	71
4.1 Introduction	71
4.2 Experimental	73
4.2.1 Device fabrication and characterization	73
4.2.2 Characterization of thin films.....	74
4.3 Result and discussion	75
4.3.1 Photovoltaic characteristics of devices.....	75
4.3.2 Optical characterization of devices and extraction of exciton diffusion length by optical modelling	78
4.3.3 Structural analysis by using X-ray spectroscopy.....	84
4.3.4 Lattice modelling by energetic consideration.....	86
4.4 Conclusion.....	90
Chapter 5 Summary and Conclusion	92
Bibliography	96
초록	105

CURRICULUM VITAE	108
List of Publications.....	111
List of Presentations.....	114
List of Patents	122

List of Tables

Table 2.1 Summary of solar cell parameters of the devices fabricated without and with CuI and MoO ₃ /CuI interfacial layers.....	39
Table 3.1 The lattice parameters of PbPc monoclinic and copper halogen compounds with zinc blende structure	61
Table 3.2 The summary of photovoltaic parameters and R_P , R_S extracted from dark J - V curves by using Shockley equation of the devices with copper halogen compounds.	68
Table 4.1 The photovoltaic parameters of the solar cells under AM 1.5G 1 sun illumination. The J_S , R_P and R_S values are extracted from dark J - V curves by using the Schokley diode equation.....	77
Table 4.2 The lattice parameters of zinc blende CuBr, monoclinic PbPc and FCC C ₇₀ are summarized.....	87

List of Figures

Figure 1.1 Schematic energy band diagram of a planar heterojunction organic photovoltaic cell. (1) Absorption of photons and creation of excitons, (2) diffusion of excitons to the interface with the acceptor, (3) dissociation of excitons into electron-hole pairs, (4) transport of electrons and holes to the electrodes and (5) collection of the carriers at the electrodes..... **7**

Figure 1.2 Typical current density-voltage characteristics of an OPV in the dark (red dashed line) and under light illumination (black solid line). The short-circuit current (J_{SC}), the open-circuit voltage (V_{OC}) are shown. The intersection between load line ($-1/R$) and J - V curve indicates the operating point of the device with load R . The maximum output power (P_{MAX}) is given by the area of the rectangle $J_{MAX} \times V_{MAX}$ **9**

Figure 1.3 Equivalent circuit of an organic photovoltaic cell. **13**

Figure 1.4 Chemical structure of typical small molecular donors which can be thermally deposited in vacuum. a) pentacene, b) metal-phthalocyanine, c) squaraine dye, d) merocyanine based dye, e) triphenylamine based molecule, f) perylene based molecule and g) dicyanovinyl-capped sexithiophene derivative. **16**

Figure 1.5 Chemical structure of typical small molecular acceptors which can be thermally deposited in vacuum. a) fullerene C_{60} , b) fullerene C_{70} , c) 3,4,9,10-perylenetetracarboxylic diimide (PTCDI)..... **19**

Figure 1.6 Chemical structure of typical small molecular hole transporting

materials which can be thermally deposited in vacuum. a) N,N'-Bis(naphthalen-1-yl)-N,N'-bis(phenyl)benzidine (NPB), b) Di-[4-(N,N -di-p-tolyl-amino)-phenyl]cyclohexane (TAPC) and the exciton blocking material bathocuproine (BCP). **20**

Figure 1.7 Schematic illustration of vacuum thermal evaporation system with various sources.. **22**

Figure 1.8 Illustration of three major growth modes. (a) island (Volmer-Weber), (b) layer-by-layer (Frank-van der Merwe) and (c) layer-plus-island (Stranski-Krastanov). **24**

Figure 1.9 Schematic representation of an overlayer on a substrate. (a) commensurate (point-on-point), (b) coincidence (point-on-line)..... **26**

Figure 1.10 Schematic representation of an overlayer on a substrate. The substrate and overlayer lattices are defined by unit cell with lattice constants \vec{a}_1 , \vec{a}_2 and α , \vec{b}_1 , \vec{b}_2 and β . The azimuthal angle θ represents the angle between the vectors \vec{a}_1 and \vec{b}_1 **28**

Figure 1.11 1-dimensional epitaxial interface between a substrate lattice and an overlayer lattice with lattice constants a and b . The potential energy of each atoms in the substrate is simply assumed as cosine function. **30**

Figure 2.1 J - V characteristics of ZnPc/C₆₀ planar heterojunction solar cells. The control device (black square) is comprised of ITO/ZnPc (25 nm)/C₆₀ (40 nm)/BCP (8 nm)/Al. The devices with a 3-nm-thick CuI (red circle) layer and also with a 3-nm-thick MoO₃/3-nm-thick CuI layer (blue triangle)

inserted between the ITO and ZnPc layers in the control device are shown.

..... **39**

Figure 2.2 The evolution of the *J-V* curves of the devices under the illumination of the AM 1.5G 100 mW cm⁻² solar simulated light for 60 minutes. (a) The control device, (b) the device with the CuI (3 nm) interfacial layer, and (c) the device with the MoO₃ (3 nm)/CuI (3 nm) interfacial layer are compared. The red square lines represent the *J-V* characteristics of the pristine samples and the blue circle lines represent the *J-V* characteristics after illumination with solar simulated light for 60 minutes. **41**

Figure 2.3 The normalized photovoltaic parameters of (a) the control device, (b) the device with the CuI (3 nm) interfacial layer, and (c) the device with the MoO₃ (3 nm)/CuI (3 nm) interfacial layer, under the illumination of solar simulated light. **43**

Figure 2.4 The evolution of the *J-V* curves of the CuI (3 nm)/control devices under the illumination of three different light sources for 30 minutes. Laser light with (a) 325 nm, (b) 442 nm, and (c) 633 nm wavelengths were used. The red square lines represent the *J-V* curves of the pristine samples and the blue circle lines represent the *J-V* curves after 30 minutes of illumination..... **44**

Figure 2.5 TOF-SIMS depth profiles of the samples in the negative mode with the structure of (a) ITO/ZnPc (25 nm)/C₆₀ (40 nm), (b) ITO/CuI (3 nm)/ZnPc (25 nm)/C₆₀ (40 nm), and (c) ITO/MoO₃ (3 nm)/CuI (3 nm)/ZnPc

(25 nm)/C₆₀ (40 nm). 47

Figure 2.6 TOF-SIMS depth profiles of the samples in the negative mode with the structure of (a) ITO/CuI (3 nm)/ZnPc (25 nm)/C₆₀ (40 nm), and (b) ITO/MoO₃ (3 nm)/CuI (3 nm)/ZnPc (25 nm)/C₆₀ (40 nm). 50

Figure 3.1 The absorption spectra of pristine 20 nm-thick PbPc film grown on ITO (black line) and films grown on 3 nm-thick CuCl (red dashed line), CuBr (blue dot line) and CuI (green dashed dot line) deposited on the ITO substrates, respectively. 57

Figure 3.2 (a) The X-ray diffraction patterns of ITO (black), PbPc (20 nm) (red), CuCl (3 nm)/PbPc (20 nm) (blue), CuBr (3 nm)/PbPc (20 nm) (green) and CuI (3 nm)/PbPc (20 nm) (pink) deposited on the ITO pre-coated glass. (b) The X-ray diffraction patterns of the films after the deposition of C₆₀ layer on top of the PbPc layer. 58

Figure 3.3 The X-ray diffraction profiles of ITO (black), ITO/CuCl (50 nm) (red), ITO/CuBr (50 nm) (blue), ITO/CuI (50 nm) (green)..... 61

Figure 3.4 (a) Schematic representation of PbPc monoclinic (320) overlayers on copper halogen compounds. The parameters a_1 , a_2 and α' of the substrates and b_1 , b_2 and β' of the PbPc layer were calculated from the lattice parameters of the respective unit cells. The azimuthal angle θ represents the angle between the vector a_1 and b_1 . (b) Calculated V/V_0 against azimuthal angle θ of PbPc overlayer on CuCl (black line), CuBr (red line) and CuI (blue line), respectively. 63

Figure 3.5 AFM images of the 5 nm-thick PbPc film grown on the ITO and

3 nm-thick CuCl, CuBr and CuI coated ITO substrate are displayed, respectively. The images are $1 \times 1 \mu\text{m}^2$ **65**

Figure 3.6 (a) The *J-V* characteristics of the OPVs with the copper halogen compounds. The control device (black square) is comprised of ITO/PbPc (20 nm)/C₆₀ (40 nm)/BCP (8 nm)/Al. The devices with a 3 nm-thick CuCl (red circle) layer, 3 nm-thick CuBr (blue triangle) and 3 nm-thick CuI (green triangle) inserted between the ITO and PbPc layers in the control device are also shown. (b) The IPCE spectra of the PbPc based control device (black square) and devices with CuCl (red circle), CuBr (blue triangle) and CuI (green triangle) are displayed. **67**

Figure 4.1 The *J-V* characteristics the OPVs with and without the CuBr layer. The control device (black square) is comprised of ITO/PbPc (20 nm)/C₇₀ (50 nm)/BCP (8 nm)/Al. The device with a 3 nm-thick CuBr (red circle) layer inserted between the ITO and PbPc layers in the control device is shown. **76**

Figure 4.2 The absorbance spectra of the films with the structures of ITO/PbPc (20 nm), ITO/CuBr (3 nm)/PbPc (20 nm) and ITO/CuBr (3 nm)/PbPc (20 nm)/C₇₀ (50 nm) are represented by the black, red and blue lines, respectively. **79**

Figure 4.3 The measured IPCE spectra of the control device (black square) and the device with the CuBr (red circle) templating layer are displayed, and the simulated IPCE spectra using the L_D values shown in the legend are also displayed by the blue lines..... **80**

Figure 4.4 (a) *J-V* characteristic curves and (b) IPCE spectra of ITO/PbPc (20 nm)/C₆₀ (40 nm)/BCP (8 nm)/Al (black square) and ITO/CuBr (3 nm)/PbPc (20 nm)/C₆₀ (40 nm)/BCP (8 nm)/Al (red triangle). **83**

Figure 4.5 (a) XRD profiles of the films with the following structures: ITO/PbPc (20 nm), ITO/CuBr (3 nm)/PbPc (20 nm), ITO/C₇₀ (50 nm), ITO/PbPc (20 nm)/C₇₀ (50 nm), and ITO/CuBr (3nm)/PbPc (20 nm)/C₇₀ (50 nm). The peaks of monoclinic PbPc with a (320) orientation and FCC C₇₀ with (111) and (220) orientations are also displayed. (b) The comparison of the peaks of the films ITO/PbPc (20 nm), ITO/CuBr (3 nm)/PbPc (20 nm) and ITO/CuBr (3 nm)/PbPc (20 nm)/C₇₀ (50 nm) near $Q = 9 \text{ nm}^{-1}$ **85**

Figure 4.6 A cartoon image of multi-layer epitaxy film comprised of ITO/CuBr/PbPc, ITO/CuBr/PbPc/C₇₀ and ITO/PbPc/C₇₀. **87**

Figure 4.7 (a) The calculated dimensionless potential V/V_0 of CuBr (111)/PbPc monoclinic (320) and PbPc monoclinic (320)/C₇₀ FCC (220). (b) Schematic representation of PbPc monoclinic (320) and C₇₀ FCC (110) unit cells on zinc blende CuBr (111). **89**

Chapter 1

Introduction

1.1 Motivation and outline of thesis

1.1.1 Motivation

The growth of world energy demand with the shortage of resources and an increase in atmospheric CO₂ urge us to find alternative energy sources. Thus, searching for environment-friendly renewable energy source is one of important task for human in this century. Earth heat, wind and tide energy are some examples of the potential of renewable sources for the production of energy. Among them, the utilization of the sunlight have been attracted due to their inexhaustible amount and eco-friendly nature. However, a large cost of production of solar panel is the limitation to replace the existing energy productions. Moreover, the shortage of rare-earth metals and handling toxic substances during fabrication are also considered as the limitation of photovoltaic industry.

Organic photovoltaic cells (OPVs) have been attracted in last decades for promising cost-effective alternative to silicon-based solar cells due to their large area applicable, low-cost, non-toxicity and flexibility advantages. Despite the the first organic photovoltaic cells were fabricated by a thermal

vacuum deposition method by C. W. Tang,¹ the solution-processed polymeric devices had been received more attention from researchers due to their simplicity in fabrication and lower price of experimental set-up compared to vacuum deposition system. OPVs comprised of polymers and fullerene derivatives show the highest power conversion efficiencies (η_p) of ~11%.² However, polymer have drawbacks for applications that they are relatively difficult to synthesis and hard to specify molecular structure. In addition, impurities during solution processing can be the origin of low batch-to-batch reproducibility and the degradation source for the device efficiency and lifetime. Instead, the small molecules attract interest in recent days because of easy purification, monodispersive molecular weight, and little batch-to-batch variations. Furthermore, small molecules can be easy to stack for the tandem architecture by using vacuum thermal deposition.

In recent days, many researchers are paying attention to the control of the crystal structure and orientation of the molecules because the optical and electrical characteristics of organic films are strongly connected with the crystal structure. One of the methods to control the crystal structure of molecules is to use a templating layer. The organic templating layers such as 3,4,9,10-perylenetetracarboxylic dianhydride (PTCDA), 2,5-bis(4-biphenyl)-bithiophene (BP2T), oxovanadium phthalocyanine (VOPc), sexithiophene (6T), para-sexiphenylene (*p*-6P), diindenoperylene (DIP) and pentacene have been used to control the crystal structure and/or the crystallinity of organic donor materials such as metal phthalocyanines.³⁻¹¹

Recently, CuI has been introduced as an effective templating material to control the crystal structure or the molecular orientation of copper phthalocyanine, zinc phthalocyanine and lead phthalocyanine (PbPc) molecules.¹²⁻²¹ The OPVs showed nearly 2 times enhancement in a η_p by inserting the CuI templating layer. However, there were few reports on the mechanism of the templating effect of the CuI layer and it is not clearly understood yet. Furthermore, the photo-stability of the solar cells with the CuI interfacial layer was very low and the devices lost their photovoltaic characteristics in a very short time under the illumination of light. For the further investigation on the templating effects, the problem in photo-stability from CuI layer had to be solved.

1.1.2 Outline of thesis

In **Chapter 1**, the framework for organic photovoltaic cells is built up and background theory to understand this thesis will be discussed. The method to interpret the performance of organic photovoltaic cells with current density-voltage (J - V) characteristic curves and incident photon-to-current efficiency (IPCE) measurement will be presented. Moreover, the theory in organic epitaxial growth in vacuum processing will be introduced. The general understanding in growth modes and the method to evaluation and prediction of epitaxial growth will be presented.

In **Chapter 2**, the photo-stability problem in the device with CuI layer

will be discussed. The poor photo-stability of the device with CuI layer raised from the diffusion of Cu which is dissociated from CuI layer under an UV light irradiation. The depth profiling by using mass spectroscopy provided the evidence of the Cu diffusion. The use of CuI and MoO₃ as a double interfacial layer between indium tin oxide (ITO) and an active layer improves the photo-stability and the templating effect of CuI was also retained.

In **Chapter 3**, the origin of the templating effects on the growth of PbPc and the performance of OPVs have been investigated by using three copper halogen compounds (CuCl, CuBr, CuI) possessing different lattice parameters as the templating layers. The crystallinity of the PbPc films was the highest on CuI followed by CuBr and CuCl, resulting in the broadening of Q-band absorption in the same order. The templating effects were able to be described by heteroepitaxial growth of organic molecules on the templating layers and the dimensionless potential calculated using a lattice model for the overlayer-substrate systems showed good correlation between the degree of epitaxy and the crystallinity of PbPc overlayers. Furthermore, the performance of OPVs was consistent with the prediction from the calculation results and the observation from the optical and structural analyses.

In **Chapter 4**, the templating effect extends to multilayers to increase the crystallinity and to modify the orientation of the crystals of PbPc and C₇₀ layers at the same time by adopting CuBr as a new templating layer on ITO.

The formations of a monoclinic phase with a preferred orientation of (320) for PbPc and a FCC phase with a preferred orientation of (220) for C₇₀ on the PbPc layer are revealed by x-ray diffraction (XRD) patterns. The multilayer epitaxy results in an increase of the exciton diffusion lengths from 5.6 nm to 8.8 nm for PbPc, and from 6.9 nm to 13.8 nm for C₇₀, to enhance the η_p of the planar heterojunction OPVs composed of PbPc and C₇₀

1.2 Organic photovoltaic cells

1.2.1 Working principles of organic photovoltaic cells

Since the first heterojunction type OPV founded by C. W. Tang, the most of the OPVs have been developed base on donor/acceptor heterojunction structure.¹ Figure 1.1 shows a schematic diagram of photocurrent generation process in organic photovoltaic cells. (1) When sunlight photons are absorbed in the active layers, tightly bounded electron-hole pairs so called 'excitons' are generated. The absorption of the acceptor is not considered here for simplicity. They cannot be dissociated to free charge carriers by thermal energy at room temperature. (2) The created excitons start to diffuse within the donor layer until they encounter the interface with acceptor. (3) There exists driving force for exciton dissociation at the donor-acceptor interface if the lowest unoccupied molecular orbital (LUMO) level of the acceptor lies lower than that of the donor and the highest occupied molecular orbital (HOMO) level of the donor lies higher than that the acceptor. The electron-hole pairs across the D/A interface still Coulombically bounded and an electric field is needed to separate them into free charges. In general, the built-in potential from the difference between the workfunction of the anode and cathode provides electric field. (4) After dissociation, free carriers are transported to electrodes. (5) Holes are collected at high work-function electrode (anode),

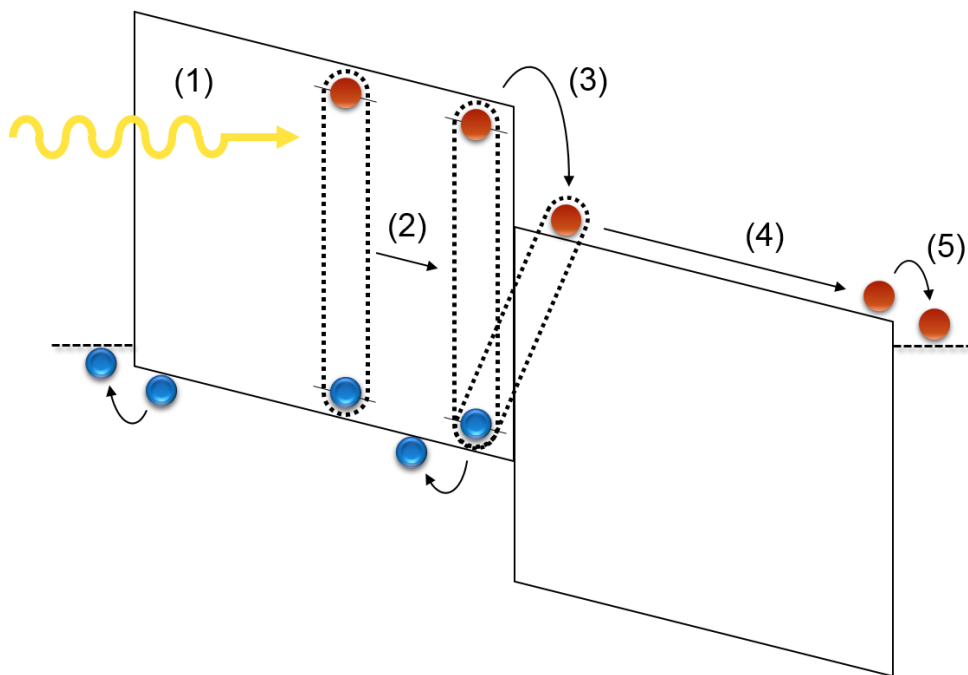


Figure 1.1 Schematic energy band diagram of a planar heterojunction organic photovoltaic cell. (1) Absorption of photons and creation of excitons, (2) diffusion of excitons to the interface with the acceptor, (3) dissociation of excitons into electron-hole pairs, (4) transport of electrons and holes to the electrodes and (5) collection of the carriers at the electrodes.

and electrons are collected at low work-function electrode (cathode).

1.2.2 Basic characterization of organic photovoltaic cells

Current density-voltage characterization

In order to investigate the performance of the organic photovoltaic cells the current density-voltage (J - V) characteristics in the dark and under light illumination are considered. In Figure 1.2, typical J - V characteristics of an OPV in the dark (red dashed line) and under light illumination (black solid line). The short-circuit current (J_{SC}) is the generated current at zero applied voltage. The open-circuit voltage (V_{OC}) is the maximum photovoltage which can be generated by the photovoltaic cell and it can be derived where current is zero under a light illumination. The intersection between load line ($-1/R$) and J - V curve indicates the operating point of the device with load R . The maximum output power (P_{MAX}) is given by the area of the rectangle $J_{MAX} \times V_{MAX}$ in quadrant III.

The short-circuit current, J_{SC} , is the generated current at zero applied voltage and is the current that flows the cell when the terminals are connected each other. Photo-generated charge carriers drifts to the electrode by internal field given by the work function difference between anode and cathode or the energy level difference between the LUMO of acceptor and the HOMO of donor. The open-circuit voltage, V_{OC} , is the maximum

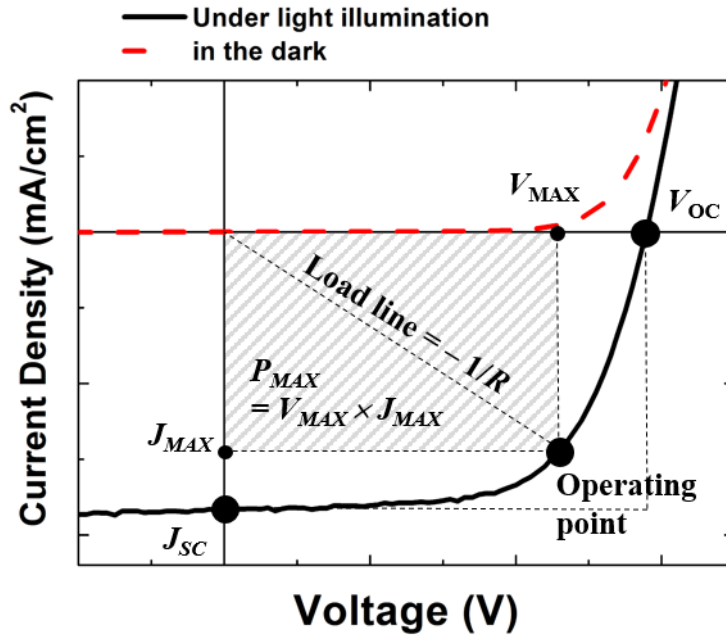


Figure 1.2 Typical current density-voltage characteristics of an OPV in the dark (red dashed line) and under light illumination (black solid line). The short-circuit current (J_{sc}), the open-circuit voltage (V_{oc}) are shown. The intersection between load line ($-1/R$) and J - V curve indicates the operating point of the device with load R . The maximum output power (P_{MAX}) is given by the area of the rectangle $J_{MAX} \times V_{MAX}$.

photovoltage which can be generated by the photovoltaic cell and it can be derived where current is zero under a light illumination. If active layers form ohmic contact to both electrodes, V_{OC} is believed to be governed by the difference between the HOMO of donor and the LUMO of acceptor. The intersection between load line ($-1/R$) and J - V curve indicates the operating point of the device with load R and the rectangle area of $J \times V$ gives generated power from the photovoltaic cell. The maximum power (P_{MAX}) generated by photovoltaic cell is located where $J \times V$ gives maximum value. This is the value that should be used to operate external circuits by organic photovoltaic cells. The fill factor, FF , is the ratio between the rectangle area of the maximum power, P_{MAX} and the product of V_{OC} and J_{SC} . It tells us the diode characteristic of the device and quality of the J - V curve.

$$FF = \frac{V_{MAX} \times J_{MAX}}{V_{OC} \times J_{SC}} \quad (1)$$

The power conversion efficiency (η_p) is defined as the ratio of the maximum electric power (P_{MAX}) to the power of the incident light (P_{input}). In our case, the incident light power is standardized to AM 1.5G, 100 mW/cm².

$$\eta_p = \frac{P_{MAX}}{P_{input}} = \frac{V_{OC} \times J_{SC} \times FF}{P_{input}} \quad (2)$$

Incident photon-to-current efficiency

The incident photon to current conversion efficiency (IPCE) is the number of photo-electrons generated per photon at each wavelength. IPCE is used equivalently with the external quantum efficiency (EQE).

$$IPCE (\%) = \frac{\# \text{ of electrons } (\lambda)}{\# \text{ of incident photons } (\lambda)} \quad (3)$$

From IPCE and the spectrum of the incident light, an upper limit of J_{SC} can be calculated.

$$J_{SC,MAX} = \int_{\lambda} \frac{hc}{q\lambda} IPCE(\lambda) I_0(\lambda) d\lambda \quad (4)$$

I_0 : the light intensity of the light source

If the recombination process takes place in the device, the J_{SC} taken from the J - V characteristic curve is lower than calculated J_{SC} from the IPCE spectrum.

Equivalent circuit

The electrical characteristics of organic photovoltaic cells can be

approximated by an equivalent circuit in Figure 1.3. In the ideal case, the J - V characteristic of a photovoltaic device under light illumination can be described by the Shockley equation.

$$J = J_s \left[\exp\left(\frac{qV}{nkT}\right) - 1 \right] - J_{ph} \quad (5)$$

The first term on the right side is the dark current density, J_s is the reverse saturation current density and n is the ideality factor of the diode. The second term on the right side is the photo-induced current, J_{ph} . For ideal case, the photo-induced current is assumed to be independent of the applied voltage. In real OPV devices, however, the photocurrent shows field dependent characteristics due to the field dependent charge dissociation and recombination.²²

In practical photovoltaic cells, the device can be represented by an equivalent circuit model shown in below. The model contains the series (R_s) and parallel (R_p) resistances. Moreover, the field dependency of the photocurrent is also considered by introducing the collection function $H(V)$.

$$J = \frac{1}{1 + R_s / R_p} \left[J_s \left\{ \exp\left(\frac{V - JR_s A}{nkT/q}\right) - 1 \right\} - \left(H(V)J_{ph} - \frac{V}{R_p A} \right) \right] \quad (6)$$

where q and k are the charge of one electron and the Boltzmann constant, and A is the area of the cell, respectively.

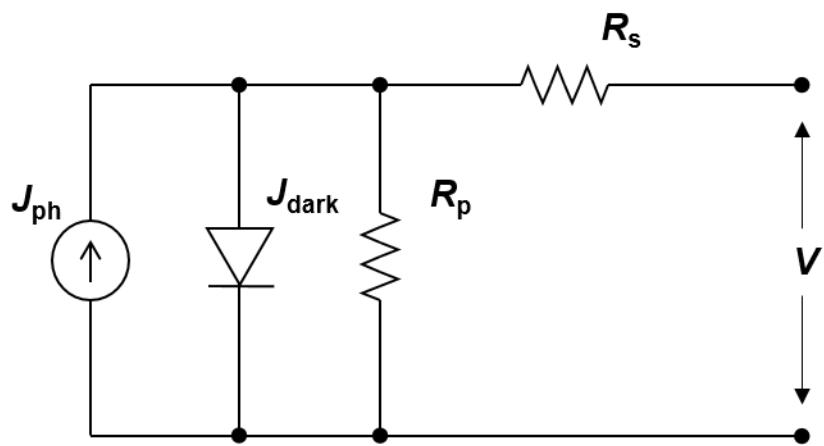


Figure 1.3 Equivalent circuit of an organic photovoltaic cell.

1.2.3 Vacuum deposited small molecular organic photovoltaic cells

As mentioned in Chapter 1, the small molecule based OPVs have attracted in recent days because of easy purification, monodisperse molecular weight, and little batch-to-batch variations. Moreover, the thermal evaporation of active materials under vacuum has been developed with several advantages and it is well already established in OLEDs industries. The vacuum processing is possible use of insoluble materials which are often more stable. It is very important merit to investigate opto-electronic characteristics of the films and the in-situ analysis with ultra-violet/x-ray photoemission spectroscopy (UPS/XPS) is also possible to analyze the electronic structure. In addition, it is possible to precise control of the thickness and deposition rate of the active layers and the active layers can be easily deposited in the form of *p-i-n* junctions or vertically gradient blends of donor-acceptor composition. By vacuum processing, furthermore, small molecules can be easy to stack for the tandem architecture by using vacuum thermal deposition. Furthermore, longer lifetime of the device is also expected because lesser impurities can be contained in the active layer during fabrication in ultra-high vacuum than solution processing. However, there is a challenge to form a bulk-heterojunction structure of donor and acceptor. In vacuum processing, co-deposited mixed layer of a donor and an acceptor has not been successful as in polymer based solar cells due to a large mixing entropy. Thus, Co-deposition does not lead to bi-continuous

interpenetrated donor-acceptor network, but rather a uniform mixture of the donor and the acceptor. The resulting isolated islands of individual materials inhibit efficient charge transport and collection. Several methods have been demonstrated in order to overcome this problem; Heating of the substrate during the deposition, thermal or solvent annealing after the deposition, alternative thermal deposition (ATD), co-deposition with additives.²³⁻²⁶

In principle, the almost infinite variety of organic materials can be synthesized for the application in organic electronic devices. Since the metal-phthalocyanine and fullerene are used as a donor and acceptor for the first heterojunction organic photovoltaic cell not many efficient small molecular materials have been reported than expected. Here in, several materials for efficient OPVs are introduced.

In Figure 1.4, representative donor materials are shown with their chemical structures. Oligoacenes are the first organic semiconducting materials from 1960. A heterojunction OPV based on pentacene with C60 was reported by Kippelen et al. In first report on pentacene based OPV, the value of η_p was 2.70% with high J_{SC} of 15 mAcm⁻². However, there was the mismatch between J_{SC} and integration of IPCE spectrum, thus it is considered as overestimated value.²⁷ Recently, η_p of 0.82% for a pentacene based OPV have been reported.²⁸ Metal-phthalocyanines have been widely used for a donor materials since C. W. Tang's the first heterojunction OPV in 1986.¹ Metal phthalocyanines have well defined crystal structure and they shows different opto-electronic characteristics and a shape by changing the

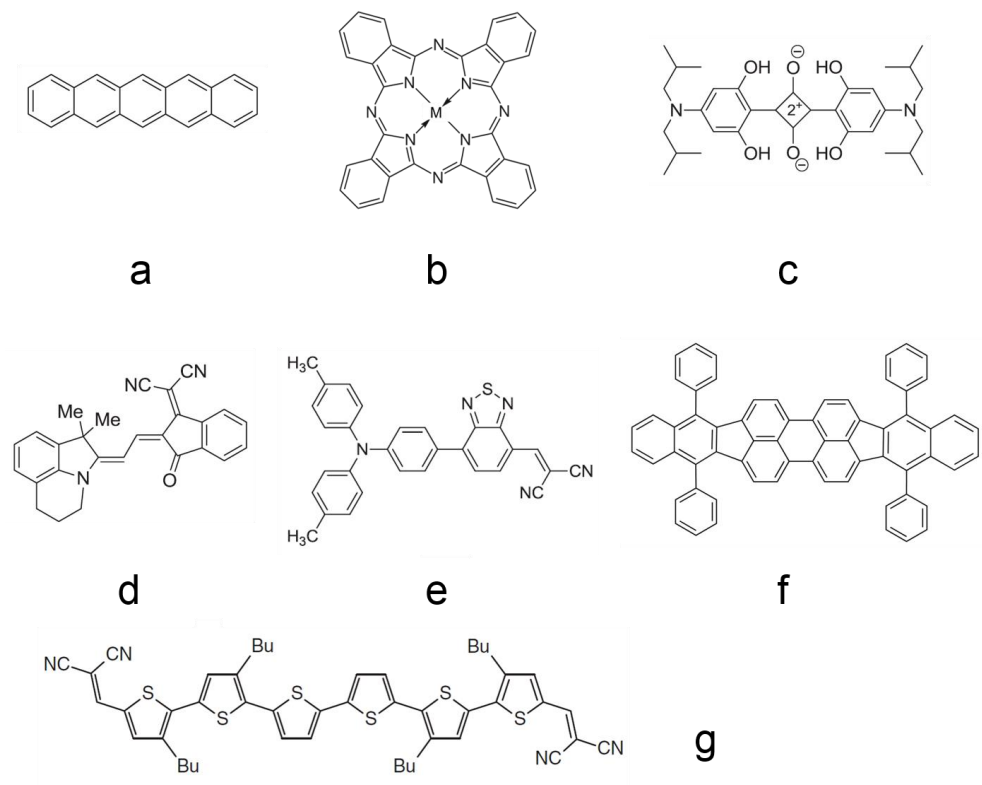


Figure 1.4 Chemical structure of typical small molecular donors which can be thermally deposited in vacuum. a) pentacene, b) metal-phthalocyanine, c) squaraine dye, d) merocyanine based dye, e) triphenylamine based molecule, f) perylene based molecule and g) dicyanovinyl-capped sexithiophene derivative.

central metal atom.

The squaraine dye-based molecules showed broad absorption from 500 to 900 nm in the film, high absorption coefficients and thermal stability. Forrest et al. developed a series of new squaraine-based dyes and squaraine dye with evaporated C₆₀ layer showed the best OPV. The performance after thermal annealing: η_p of 5.7%, J_{SC} of 10.0 mA cm⁻², V_{OC} of 0.90 V, and FF of 0.64.²⁹

Merocyanine dye based molecules have attracted for a donor materials due to the high absorption coefficient and the large variability in the value of HOMO and LUMO levels. Würthner et al. reported the OPV with high η_p of 6.10% with high V_{OC} of 0.962 V.³⁰

Wong et al. have reported a D-A system in which the triphenylamine block is connected to a dicyanovinyl acceptor by a dithienosilole group. They synthesized the new triphenylamine based donor molecule and fabricated the OPV with η_p of 6.80% by codeposition in vacuum with C₇₀ as an acceptor material.³¹ Recently, Forrest et al. reported the highest η_p of 11.1% multijunction OPV.² The triphenylamine based DTDCTB molecule and perylene based DBP were used for absorbing the near IR region and visible region, respectively.

The dicyanovinyl group shows efficient intramolecular charge transfer with oligothiophenes due to strong electron-withdrawing property. Leo et al. reported the η_p of 6.07% using multijunction structure.³²

Fullerenes and their derivatives have been widely used in OPVs due to their

proper energy level and high electron mobility. In general, C₆₀ and C₇₀ have been used in vacuum process. However, deep LUMO level of C₆₀ and C₇₀ leads to small V_{OC} of OPVs. Recently, indene bisadduct (ICBA) were synthesized and it has ~0.2 eV up-shifted LUMO level. Thus the OPV with indene-fullerene bisadduct shows higher V_{OC}.^{33,34}

Perylene based acceptors have been attracted as alternative acceptor material, however the performance is still lower.³⁵

To overcome the poor charge transport in organic layers and energetic barrier for the charge extraction, *p-i-n* structure have been used in OPVs. In Figure 1.6, N,N'-Bis(naphthalen-1-yl)-N,N'-bis(phenyl)benzidine (NPB), b) Di-[4-(N,N -di-p-tolyl-amino)-phenyl]cyclohexane (TAPC) which are representative hole transporting materials are displayed. Furthermore, exciton blocking layer is needed to prevent the formation of complex of fullerene and metal electrode. The complex of fullerene and metal forms the dipole at the interface and it obstruct the carrier extraction. Most of small molecule based OPV have the exciton blocking layer and bathocuproine (BCP) is widely used.

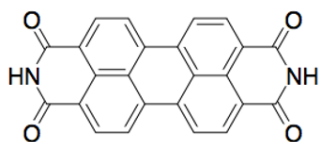
The ultra-high vacuum chamber is needed for the thermal deposition. A schematic drawing of the vacuum chamber is shown in Figure 1.7. The organic materials are stored in Al₂O₃ crucible with a heating coil under ~10⁻⁷ torr. The organic materials can be sublimated above their sublimation temperature. Generally, molecules move in a straight line and form the film when the cold side not only a substrate but also walls. Thus shutters for the



a



b



c

Figure 1.5 Chemical structure of typical small molecular acceptors which can be thermally deposited in vacuum. a) fullerene C_{60} , b) fullerene C_{70} , c) 3,4,9,10-perylenetetracarboxylic diimide (PTCDI).

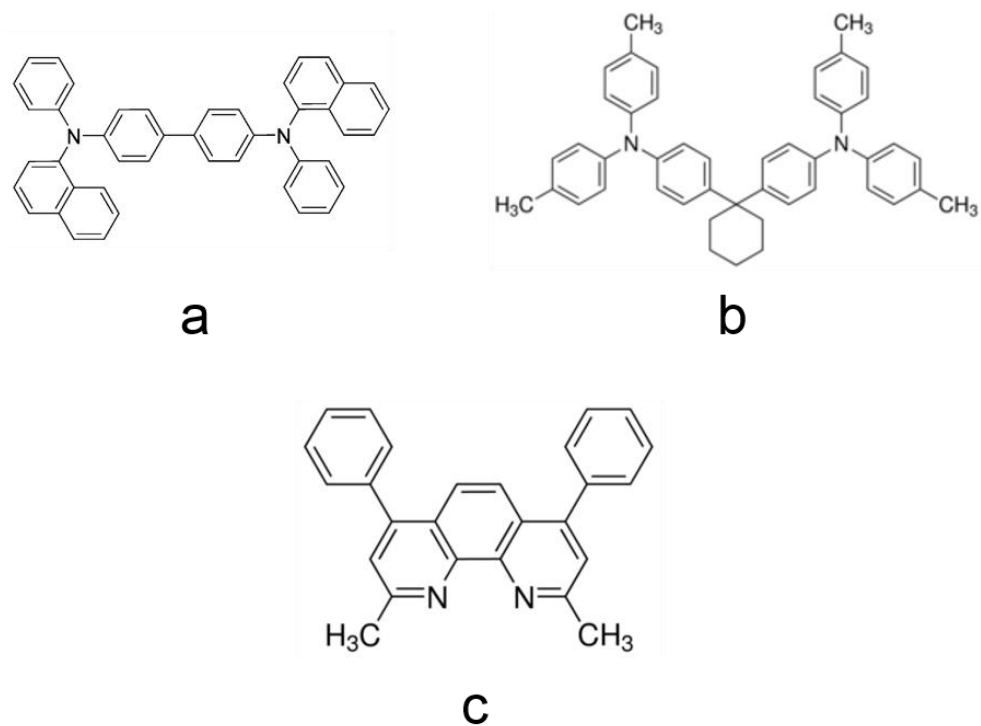


Figure 1.6 Chemical structure of typical small molecular hole transporting materials which can be thermally deposited in vacuum. a) N,N'-Bis(naphthalen-1-yl)-N,N'-bis(phenyl)benzidine (NPB), b) Di-[4-(N,N -di-p-tolyl-amino)-phenyl]cyclohexane (TAPC) and the exciton blocking material bathocuproine (BCP).

source and substrate and the deposition rate have to be monitored by quartz crystal microbalance (QCM) sensor. The substrate has to be rotated for the film uniformity. The completed devices are transferred to glove box and encapsulated under N₂ environment.

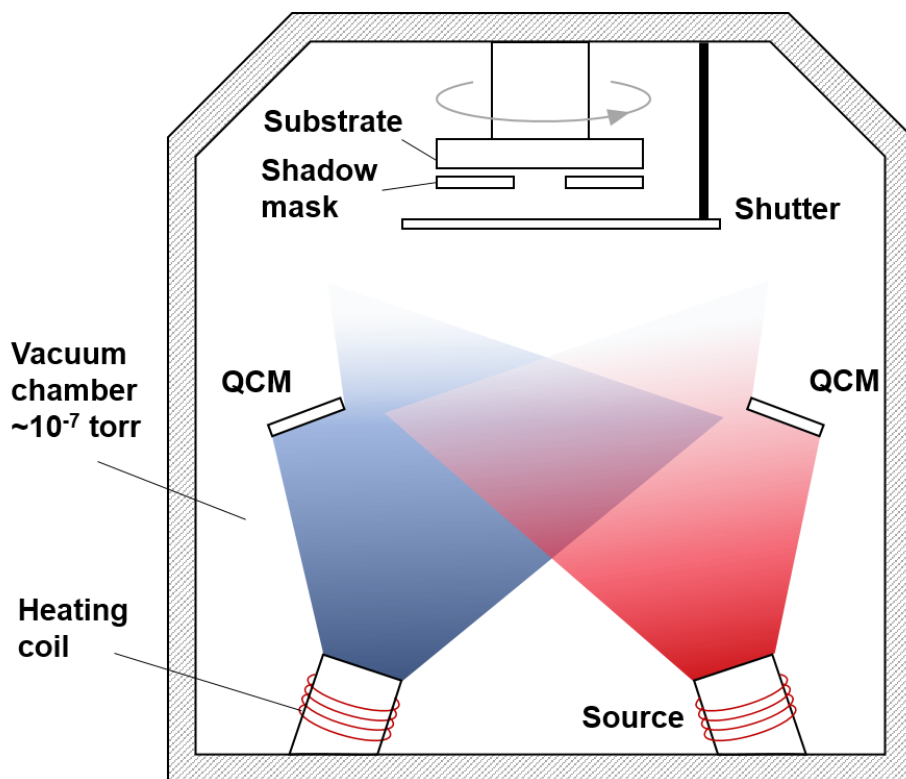


Figure 1.7 Schematic illustration of vacuum thermal evaporation system with various sources.

1.3 Epitaxial growth of organic molecules and simple lattice modelling

1.3.1 Epitaxial growth of organic molecules

Epitaxy refers to the oriented crystalline growth of overlayer on the crystalline substrate. The term 'epitaxy' comes from the Greek words *epi* (above) and *taxis* (in ordered manner), that stands for the arranged overlayer on the surface of substrates.³⁶ Almost inorganic semiconductor based electronic devices such as GaN, AlGaInP or GaP based light emitting diodes (LEDs) have multilayered structure, thus, deep comprehension on crystalline growth of thin film on various substrates is important to achieve high crystalline thin films and high performance. Therefore, many researchers have been studied about epitaxial growth and the have been established well in inorganic materials.

Generally, the thin film growth modes can be described with three major models illustrated in Figure 1.1: (1) island (Volmer-Weber), (2) layer-by-layer (Frank-van der Merwe) and (3) layer-plus-island (Stranski-Krastanov). Volmer-Weber growth mode occurs when the deposited atoms or molecules are more strongly bonded each other than interaction with substrates. The atoms or molecules nucleated on the surface and they grow into three-dimensional islands. Frank-van der Merwe growth mode can be

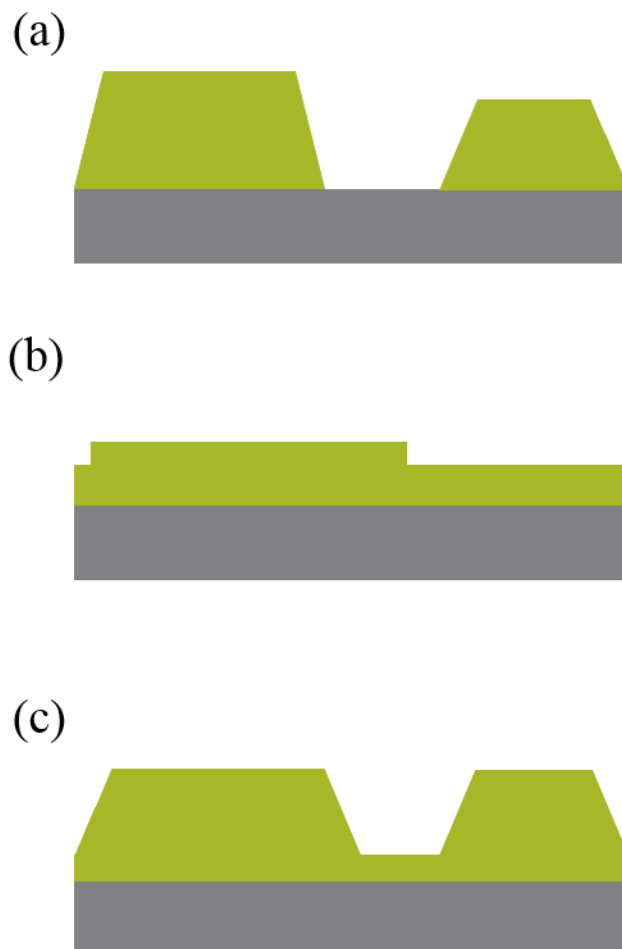


Figure 1.8 Illustration of three major growth modes. (a) island (Volmer-Weber), (b) layer-by-layer (Frank-van der Merwe) and (c) layer-plus-island (Stranski-Krastanov).

occurred when opposite condition. In case of the interaction between the deposited atoms or molecules and substrates is stronger than bonding each other, they grow in layer-by-layer structure like sheet feature. Stranski-Krastanov mode is a combination of the above two growth modes. In this growth mode, the one or several monolayers are initially formed in a layer-by-layer, they become energetically unfavorable and islands begin to growth.

In case of organic materials, the epitaxial growth have been studied in the research field of organic molecular beam deposition (OMBD) or organic molecular beam epitaxy (OMBE) in the 1980s. Generally, organic molecules have lower symmetry and larger lattice constant than inorganic materials, thus commensurate growth is hard to be found. Forrest et al. proposed the coincident epitaxy and incommensurate epitaxy which are occurred although the lack of commensurability.³⁷ The 'commensurate' is the condition when the every overlayer lattice site on the substrate lattice and it is generally energetically most favorable. This is so called "point-on-point" coincidence and schematic representation is illustrated in Figure 1.2a. In Figure 1.2b, "point-on-line" coincidence is displayed. It is energetically favorable when the lattice vector of the overlayer can be described as an integer multiplication of the lattice vector of the substrate. If there is no distinctive registry between the overlayer lattice and the substrate, it is called incommensurate epitaxy structure. The growth of metal-phthalocyanines on the ionic compounds such as KBr and NaCl is one of examples of coincidence epitaxy.^{38,39} In addition, perylenetetracarboxylic

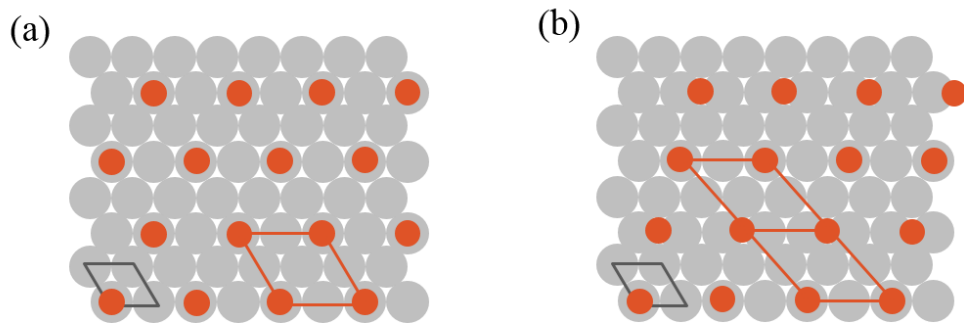


Figure 1.9 Schematic representation of an overlayer on a substrate. (a) commensurate (point-on-point), (b) coincidence (point-on-line)

dianhydride (PTCDA) can be grown as the coincidence epitaxy on the ionic substrate, cleaved metal surface and highly oriented pyrolytic graphite (HOPG).^{40,41}

1.3.2 Energetic consideration and simple lattice modelling

The possibility of an epitaxial relationship between an overlayer and substrate can be predicted by calculating the potential energy. For determining the optimum epitaxial configuration, so many interactions, such as chemisorption, dispersive and electrostatic interactions, are typically modeled with a Morse potential, Lennard-Jones or Buckingham potentials.⁴²⁻⁴⁴ However, considering the interaction of every atoms in the overlayer and substrate is not easy to computing. Ward et al. proposed a computationally efficient geometric lattice misfit algorithm which uses only the lattice parameters of the overlayer and substrate as input.⁴⁵ Their approach can provide meaningful insight to predict and understand the growth modes despite of their model cannot reflect the details of physical structure of the molecules and they cannot predict the preferred orientation of molecules.

Epitaxy generally describes the lattice registry or the degree of phase matching between an overlayer and a substrate lattice. For the 1-dimension, the lattice misfit can be expressed with the misfit parameter $f = (b - a)/a$

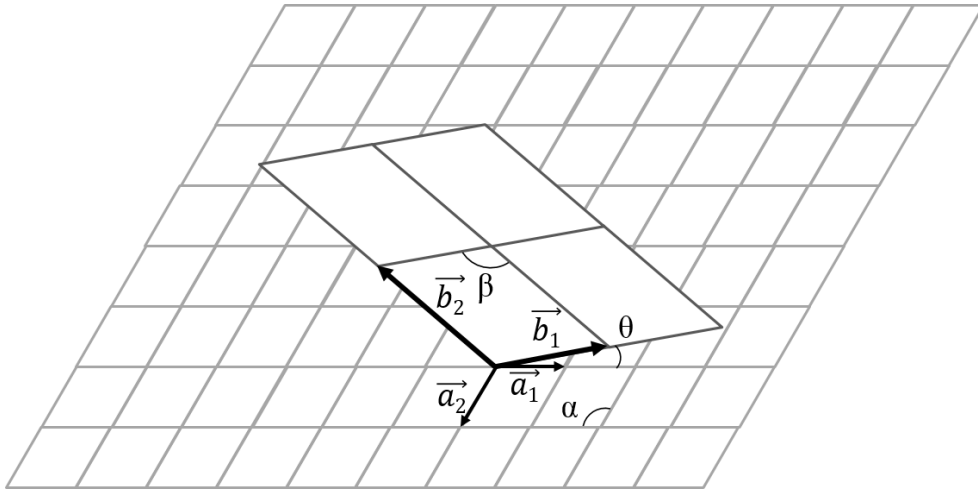


Figure 1.10 Schematic representation of an overlayer on a substrate. The substrate and overlayer lattices are defined by unit cell with lattice constants \vec{a}_1 , \vec{a}_2 and α , \vec{b}_1 , \vec{b}_2 and β . The azimuthal angle θ represents the angle between the vectors \vec{a}_1 and \vec{b}_1 .

where a and b are lattice constants of overlayer and substrate. However, more parameters are needed when a two-dimensional interface is considered. The two-dimensional interface consisting of the overlayer and the substrate is displayed in Figure 1.3. The substrate and overlayer lattices are defined by unit cell with lattice constants \vec{a}_1 , \vec{a}_2 and α , \vec{b}_1 , \vec{b}_2 and β , respectively. The azimuthal angle θ represents the angle between the vectors \vec{a}_1 and \vec{b}_1 . The azimuthal relationship between the substrate and the overlayer can be described by a transformation matrix \mathbf{C} . The matrix \mathbf{C} consists with elements p_x , q_y , q_x and p_y .

$$\begin{bmatrix} \vec{b}_1 \\ \vec{b}_2 \end{bmatrix} = [\mathbf{C}] \begin{bmatrix} \vec{a}_1 \\ \vec{a}_2 \end{bmatrix} = \begin{bmatrix} p_x & q_y \\ q_x & p_y \end{bmatrix} \begin{bmatrix} \vec{a}_1 \\ \vec{a}_2 \end{bmatrix} \quad (1)$$

$$p_x = b_1 \sin(\alpha - \theta) / a_1 \sin \alpha \quad (2)$$

$$q_y = b_1 \sin \theta / a_2 \sin \alpha \quad (3)$$

$$q_x = b_2 \sin(\alpha - \theta - \beta) / a_1 \sin \alpha \quad (4)$$

$$p_y = b_2 \sin(\theta + \beta) / a_2 \sin \alpha \quad (5)$$

Ward et al. proposed the dimensionless potential energy V/V_0 for the evaluating the epitaxy which can be obtained by an analytical method. For the 1-dimensional interface between the overlayer lattice and the substrate illustrated in Figure 1.4. The substrate lattice and the overlayer lattice have lattice constants a and b . When the potential energy of each atoms in the substrate is simply assumed as cosine function, an 1-dimensional V/V_0 can

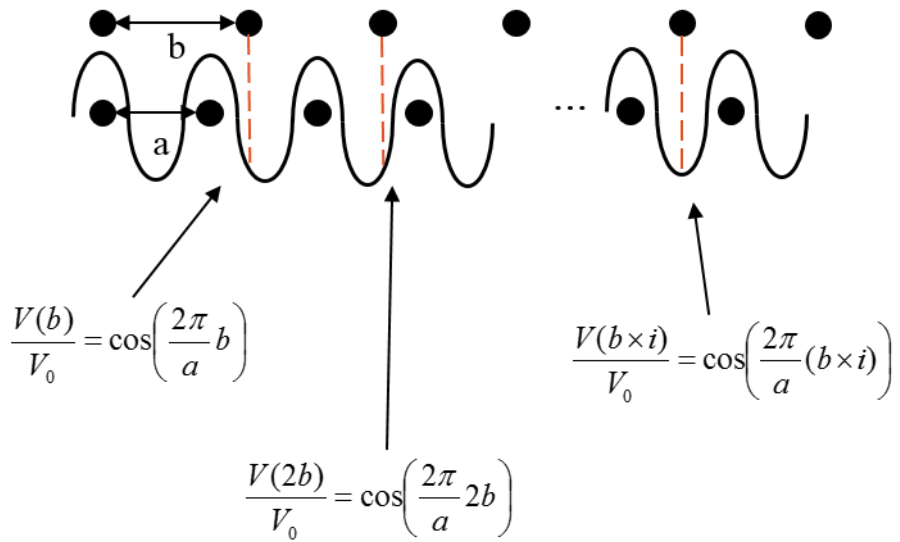


Figure 1.11 1-dimensional epitaxial interface between a substrate lattice and an overlayer lattice with lattice constants a and b . The potential energy of each atoms in the substrate is simply assumed as cosine function.

be described by Eq. (6).

$$\frac{V(x)}{V_0} = \cos\left(\frac{2\pi}{a}x\right) \quad (6)$$

The total dimensionless potential V/V_0 can be obtained by the summation of the potential energy of the atoms, and it can be described by Eq. (7).

$$\frac{V}{V_0} = \frac{\sum_i \left[1 - \cos\left(\frac{2\pi b}{a}i\right) \right]}{\sum_i} \quad (7)$$

$i = 0, \pm 1, \dots, \pm m$

The Eq. (7) can be easily derived to Eq. (8) mathematically.

$$\frac{V}{V_0} = \left[(2m+1) - \frac{\sin(2m+1)\pi(f+1)}{\sin\pi(f+1)} \right] \left(\frac{1}{2m+1} \right) \quad (8)$$

From Eq. (8), when the misfit parameter f increases the dimensionless potential V/V_0 also increases and when the misfit parameter $f = 0$, V/V_0 also have the value of 0.

This approach can be extended to the two-dimensional interface between the overlayer and substrate. The dimensionless potential can be described by Eq. (9) with the transformation matrix \mathbf{C} .

$$\frac{V}{V_0} = \frac{\frac{1}{2} \sum_i \sum_j \left\{ 2 - \cos \left[2\pi(ij) \begin{bmatrix} C \\ 1 \\ 0 \end{bmatrix} \right] - \cos \left[2\pi(ij) \begin{bmatrix} C \\ 0 \\ 1 \end{bmatrix} \right] \right\}}{\sum_i \sum_j} \quad (9)$$

The analytic function of Eq. (9) can be derived with the terms of M and N which correspond to the multiples of overlayer unit cell vector \vec{b}_1 and \vec{b}_2 of the $\mathbf{M} \times \mathbf{N}$ unit cell.

$$\frac{V}{V_0} = \left\{ 2MN - \frac{\sin(M\pi p_x) \sin(N\pi q_x)}{\sin(\pi p_x) \sin(\pi q_x)} - \frac{\sin(M\pi q_y) \sin(N\pi p_y)}{\sin(\pi q_y) \sin(\pi p_y)} \right\} \left(\frac{1}{2MN} \right) \quad (10)$$

$$M = 2m + 1$$

$$N = 2n + 1$$

The dimensionless potential V/V_0 can be calculated for azimuthal orientations and evaluating the azimuthal angle with the optimum phase matching condition can be obtained by Eq. (10).

Chapter 2

High efficiency and high photo-stability zinc-phthalocyanine based planar heterojunction solar cells with a double interfacial layer

2.1 Introduction

Organic photovoltaic cells (OPVs) comprised of polymers and fullerene (C_{60}) derivatives show the highest power conversion efficiencies (η_p) of $\sim 8\%$.⁴⁶⁻⁵¹ However, small molecules attract interest in recent days because of easy purification, monodisperse molecular weight, and little batch-to-batch variations. Moreover, η_p values of small molecule based photovoltaic cells have been improved up to 7% and these values are close to polymer based devices.^{30,32,52-58}

Metal-phthalocyanines (MPcs) and C_{60} are very classical materials and widely used as donor and acceptor molecules, respectively, for small molecular planar heterojunction OPVs. However, MPc/ C_{60} based small molecular planar heterojunction photovoltaic cells show low η_p of 1~2% and short lifetimes.⁵⁹⁻⁶⁵ Recently, the co-deposition of donor and acceptor materials have been used to improve η_p by making bulk heterojunction (BHJ) structures comprised of small molecules. However, co-deposited

layers of small molecules have not been so successful to form BHJ structures as in polymer solar cells due to a large entropy of mixing to reduce the tendency towards phase separation, and the devices shows η_p values of 2~3%.^{25,59,61-65}

Moreover, MPC/C₆₀ planar heterojunction solar cells showed the characteristics of photo-degradation under the illumination of light even for a short time range in a nitrogen environment. A few mechanisms have been proposed to explain the photo-degradation characteristics, including the formation of a gap state at the interface of the donor and acceptor by the photo-reaction of C₆₀ with oxygen, the photo-assisted diffusion of the oxygen from indium-tin-oxide (ITO) to the donor layer, and a reduced work function of the ITO by UV light.⁶⁶⁻⁶⁸ Recently, it was proposed that insertion of a molybdenum oxide (MoO₃) layer at the interface between the ITO and donor which would act as a barrier for oxygen diffusion could increase the photo-stability of the devices.⁶⁹⁻⁷¹ However, the researchers could not give direct evidence of the hypothesis and further investigation is needed to understand the photo-degradation mechanism in planar heterojunction devices for a tremendous improvement in cell lifetimes.

Recently CuI has been used as a template material for the horizontal stacking of copper-phthalocyanine, zinc-phthalocyanine (ZnPc) and lead-phthalocyanine molecules.^{12,13,15,18,19} CuI was previously used as a hole injection material in OLED devices.⁷² Horizontally stacked MPC films showed an enhancement in the absorption coefficient resulting in the

improved power conversion efficiency of the solar cells.^{3,5,73} However, the photo-stability of the solar cells with the CuI interfacial layer was very low and the devices lost their photovoltaic characteristics in a very short time under the illumination of light.

Herein, we report that the use of MoO₃ and CuI as a double interfacial layer improves the η_p value and the photo-stability in ZnPc based solar cells at the same time. Furthermore, we investigated the origin of the photo-degradation of the device with CuI and the role of the MoO₃ layer for high photo-stability by using time-of-flight secondary ion mass spectrometry (TOF-SIMS).

2.2 Experimental

2.2.1 Device fabrication and characterization

The control device had the following simple structure: indium tin oxide (ITO) (150 nm)/ ZnPc (25 nm)/ C₆₀ (40 nm)/ BCP (8 nm)/ Al (100 nm). The 150 nm thick ITO coated glass substrate was successively cleaned with acetone and isopropylalcohol. The substrate was exposed to UV-O₃ for 10 min before use. All the organic layers were deposited using thermal evaporation at the base pressure of ca. 10⁻⁷ Torr with a rate of 1 Å/s. The 100 nm-thick Al cathode was deposited at a rate of 4 Å/s. MoO₃ and CuI layers were deposited onto the substrate with a rate of 0.2 Å/s. All the layers were successively evaporated without breaking the vacuum. The devices had active areas of 4 mm². A patterned insulator on the ITO and the top cathode deposited through a shadow mask defined the cell area. After fabrication, the devices were encapsulated using epoxy resin with glass cans in an N₂ environment. The photovoltaic properties of the devices were measured with an AM 1.5G 100 mW cm⁻² solar simulator (300 W Oriel 69911A) light source and a source measurement unit (Keithley 237). The measurement set up was calibrated with a National Renewable Energy Laboratory-certified reference Si-solar cell covered with a KG-5 filter before every measurement.

2.2.2 Device aging condition

The devices were aged under the illumination of light of various wavelengths in an N₂ environment. The AM 1.5G 100 mW cm⁻² simulated solar light used a 4 mW cm⁻² of 633 nm *HeNe* laser light (Auburn) and also 3.6 mW cm⁻² of 442 nm and 3.9 mW cm⁻² of 325 nm *HeCd* laser light (Omnichrome, Series 56), and in addition a 15 mW cm⁻² metal halide UV lamp were used as the light sources.

2.2.3 Depth profiling

Depth profiling of the mass spectra of the devices were performed by using a TOF-SIMS 5 (ION TOF GmbH). 0.9 pA of 25 keV Bi⁺ was used as the primary ion to obtain the mass spectra. The mass spectra were obtained on an area of 50×50 μm². For depth profiling, 31 nA of 0.5 keV Cs⁺ ion was used for sputtering. The sputtered area was 200×200 μm². Samples were fabricated onto 0.1×0.1 cm² of ITO glass substrates. The ITO glass substrates were cleaned using the same procedure as was used for the device cleaning. ZnPc and C₆₀ layers were thermally deposited onto the substrates at a base pressure of ca. 10⁻⁷ Torr with a rate of 1 Å/s. MoO₃ and CuI films were evaporated with a rate of 0.2 Å/s. All the layers were successively evaporated without breaking the vacuum.

2.3 Result and Discussion

2.3.1 Current density-voltage characteristics

The current density-voltage (J - V) characteristics of the solar cells under AM 1.5G illumination (100 mW cm^{-2}) are shown in Figure 2.1. The control device is comprised of ITO/ZnPc (25 nm)/C₆₀ (40 nm)/bathocuproine (BCP) (8 nm)/ Al. The 150 nm thick ITO coated glass substrate was successively cleaned with acetone and isopropylalcohol. The substrate was exposed to UV-O₃ for 10 min before use. All the organic layers were deposited using thermal evaporation at the base pressure of ca. 10^{-7} Torr with a rate of 1 \AA/s . The 100 nm-thick Al cathode was deposited at a rate of 4 \AA/s . MoO₃ and CuI layers were deposited onto the substrate with a rate of 0.2 \AA/s . All the layers were successively evaporated without breaking the vacuum. The devices had active areas of 4 mm^2 . After fabrication, all the devices were encapsulated using epoxy resin with glass cans in an N₂ environment. The photovoltaic properties of the devices were measured with an AM 1.5G 100 mW cm^{-2} solar simulator (300 W Oriel 69911A) light source and a source measurement unit (Keithley 237). The measurement set up was calibrated with a National Renewable Energy Laboratory-certified reference Si-solar cell covered with a KG-5 filter before every

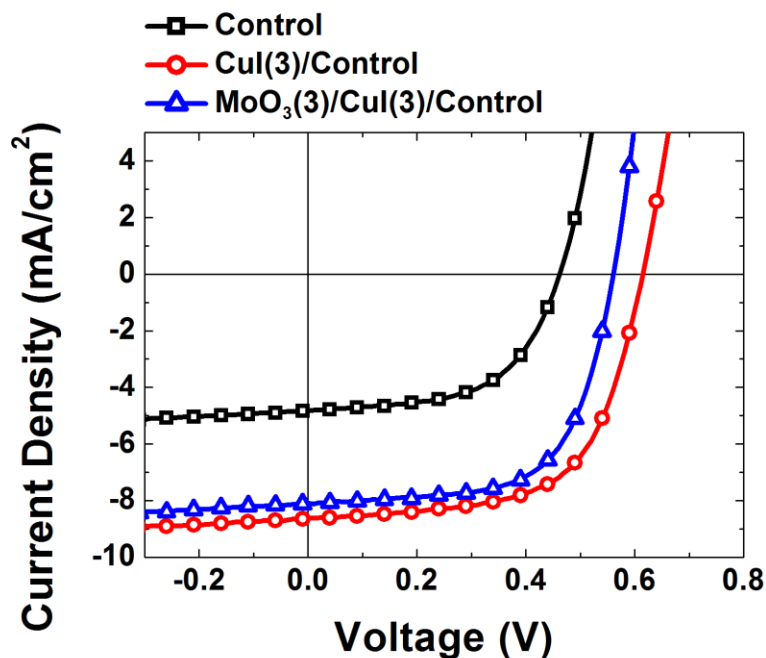


Figure 2.1 *J-V* characteristics of ZnPc/C₆₀ planar heterojunction solar cells.

The control device (black square) is comprised of ITO/ZnPc (25 nm)/C₆₀ (40 nm)/BCP (8 nm)/Al. The devices with a 3-nm-thick CuI (red circle) layer and also with a 3-nm-thick MoO₃/3-nm-thick CuI layer (blue triangle) inserted between the ITO and ZnPc layers in the control device are shown.

Table 2.1 Summary of solar cell parameters of the devices fabricated without and with CuI and MoO₃/CuI interfacial layers.

Device	η_p [%]	J_{sc} [mA cm ⁻²]	V_{oc} [V]	FF
Control	1.27	4.83	0.46	0.57
CuI (3 nm)	3.30	8.63	0.61	0.62
MoO ₃ (3 nm)/ CuI (3 nm)	2.89	8.19	0.56	0.63

measurement. The control device showed a η_p of 1.27% with a short-circuit current density (J_{SC}) of 4.83 mA cm⁻², an open-circuit voltage (V_{OC}) of 0.46 V and a fill factor (FF) of 0.57, which is similar to the previous reports. The insertion of a 3-nm-thick CuI layer between the ITO and ZnPc remarkably enhanced the performance of the solar cell resulting in a η_p value of 3.30% with a J_{SC} of 8.63 mA cm⁻², a V_{OC} of 0.61 V and an FF of 0.62. The device characteristics are summarized in Table 2.1. The J - V characteristic of the device with the MoO₃ (3 nm)/CuI (3 nm) double interfacial layer is also included in Figure 2.1. The device shows a lower performance than the device containing the CuI interfacial layer only, with $\eta_p = 2.89%$, $J_{SC} = 8.19$ mA cm⁻², $V_{OC} = 0.56$ V and $FF = 0.63$. Nevertheless, the performance of the device is more than two times higher than the performance of the control device containing no interfacial layers.

2.3.2 Photo-stability of devices

The photo-stability of the encapsulated devices was examined by measuring the J - V characteristics every 5 minutes under AM 1.5G illumination (100 mW cm⁻²) of light for 60 minutes. The results are displayed in Figure 2.2 and Figure 2.3. The ‘S-shaped kink’ was developed in the J - V curve of the control device upon illumination of the AM 1.5G simulated light leading to the degradation of the performance

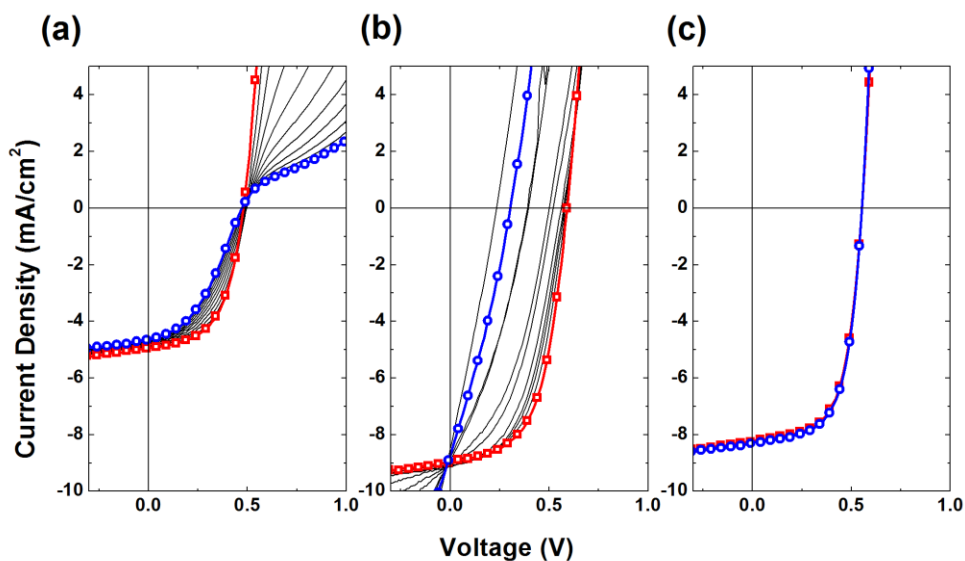


Figure 2.2 The evolution of the J - V curves of the devices under the illumination of the AM 1.5G 100 mW cm^{-2} solar simulated light for 60 minutes. (a) The control device, (b) the device with the CuI (3 nm) interfacial layer, and (c) the device with the MoO₃ (3 nm)/CuI (3 nm) interfacial layer are compared. The red square lines represent the J - V characteristics of the pristine samples and the blue circle lines represent the J - V characteristics after illumination with solar simulated light for 60 minutes.

(Figure 2.2a). After 60 minutes of illumination, η_p decreased to below 70% of the initial value mainly due to the reduction of FF without significant changes in J_{SC} and V_{OC} (Figure 2.3a). This behavior may be explained by the lowering of the work function of ITO by the irradiation of UV light and the formation of an injection barrier at the interface between the ITO and the ZnPc layer. The evolution of the J - V characteristics of the device with a CuI interfacial layer under illumination shows very different degradation behavior from the control device (Figure 2.2b). The shunt resistance of the device is rapidly reduced under illumination, leading to the decrease of FF and V_{OC} . This fact indicates that the p - n junction characteristic of the device was lost due to the formation of another charge transport path by the irradiation of light. As shown in Figure 2.3b, the η_p value of the device with the CuI interfacial layer was reduced to $\sim 30\%$ of the initial value after the illumination of the solar simulated light for 60 minutes. In contrast, the device with MoO₃/CuI double interfacial layer showed high photo-stability under the same illumination conditions. As shown in Figure 2c and Figure 2.3c, little change in the J - V characteristics was observed under the illumination of light for 60 minutes, demonstrating a significantly higher photo-stability than was seen for the other two devices.

To understand the mechanism of the photo-degradation of the CuI layer containing device, the wavelength dependent photo-degradation of

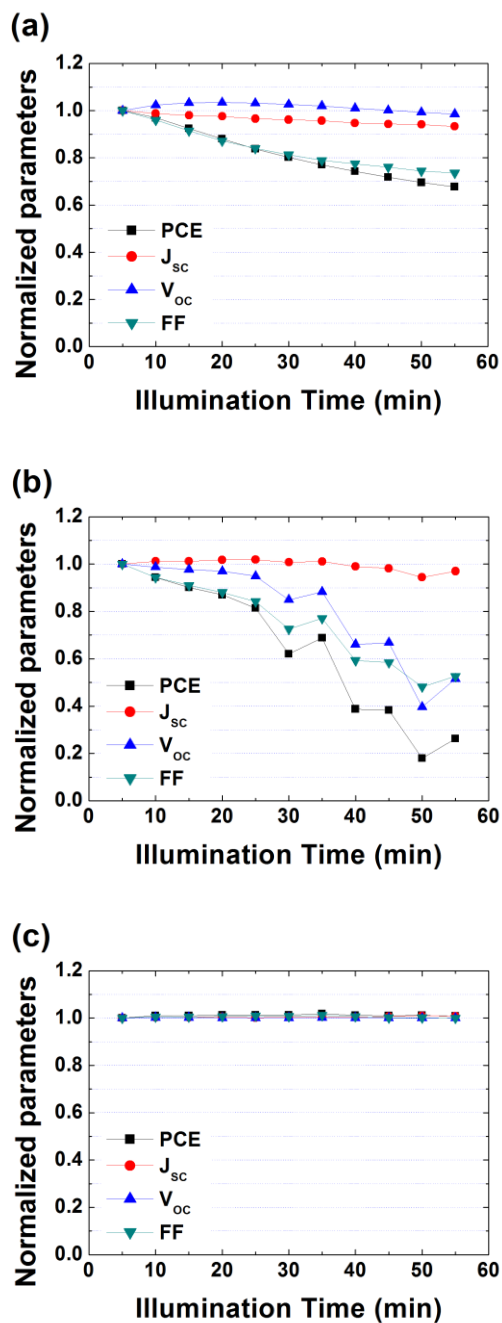


Figure 2.3 The normalized photovoltaic parameters of (a) the control device, (b) the device with the CuI (3 nm) interfacial layer, and (c) the device with the MoO₃ (3 nm)/CuI (3 nm) interfacial layer, under the illumination of solar simulated light.

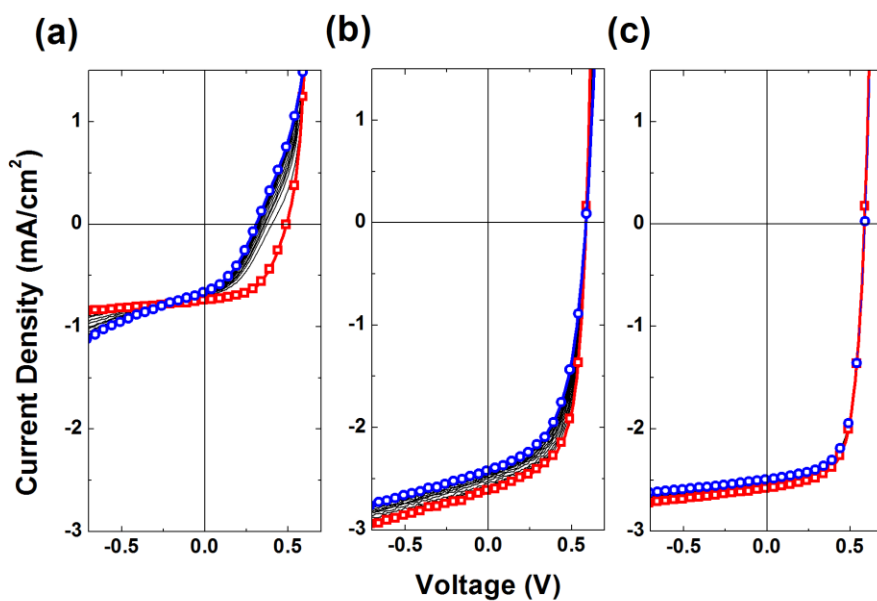


Figure 2.4 The evolution of the J - V curves of the CuI (3 nm)/control devices under the illumination of three different light sources for 30 minutes. Laser light with (a) 325 nm, (b) 442 nm, and (c) 633 nm wavelengths were used. The red square lines represent the J - V curves of the pristine samples and the blue circle lines represent the J - V curves after 30 minutes of illumination.

the device was investigated using three different light sources for photocurrent generation: 4 mW cm^{-2} of 633 nm HeNe laser light; 3.6 mW cm^{-2} of 442 nm HeCd laser light; and 3.9 mW cm^{-2} of 325 nm HeCd laser light. The wavelengths of the light were selected to identify the materials inducing the degradation since the HeNe laser light is only absorbed by ZnPc, 442 nm light mainly by C_{60} and 325 nm light by ITO. The J - V characteristics of the devices after illumination by the laser for 30 minutes are shown in Figure 2.4. The results clearly exhibit that the degradation characteristics strongly depend on the wavelength of the illuminating light. Irradiation by the 633 nm laser light does not degrade the device at all. Since the 633 nm light is mostly absorbed by ZnPc, this fact indicates that excitation of the ZnPc does not degrade the device. In the case of irradiation by the 442 nm laser, a decrease of FF and V_{OC} was not observed. In contrast, FF and V_{OC} of the device were reduced by irradiation of the device with the 325 nm laser light. These results indicate that the photo-degradation in the CuI containing device mainly originates from the UV-induced reaction of CuI at the interface with the ITO.

2.3.3 Depth profiling by using Time-of-Flight-Secondary Ion Mass Spectroscopy

Further investigation was carried out by TOF-SIMS (TOF-SIMS 5;

ION TOF GmbH) to reveal the origin of the degradation.^{65,74,75} 0.9 pA of 25 keV Bi⁺ was used as the primary ion to obtain the mass spectra. The mass spectra were obtained on an area of 50×50 μm². For depth profiling, 31 nA of 0.5 keV Cs⁺ ion was used for sputtering. The sputtered area was 200×200 μm². Samples were fabricated onto 0.1×0.1 cm² of ITO glass substrates. Figure 2.5 shows the TOF-SIMS depth profiles of the samples. The samples had the following structures: ITO/ZnPc (25 nm)/C₆₀ (40 nm); ITO/CuI (3 nm)/ZnPc (25 nm)/C₆₀ (40 nm); and ITO/MoO₃ (3 nm)/CuI (3 nm)/ZnPc (25 nm)/C₆₀ (40 nm), which were fabricated using the same procedure described before. All the samples were aged under a 15 mW cm⁻² metal halide UV light source and compared with pristine samples. Figure 2.5a displays the depth profile of the reference sample. C₂N₂Cs⁻ and ZnC₂N₂⁻ are the markers for the ZnPc layer. The C⁻ ion was selected as the marker for the C₆₀ layer and the decline of C⁻ is consistent with increase in the markers of the ZnPc layer. Thus, we could define the interface between C₆₀ and ZnPc at the sputtering time of ~450 s. By using In⁻ as the marker for ITO, the interface between the ZnPc and ITO was defined at the time of ~550 s. Any notable changes in the depth profiles were not observed from the aged sample compared with the pristine sample in the mass spectra of the selected ions. The depth profiles of the samples containing a 3-nm-thick CuI layer are displayed in Figure 2.5b. C₂N₂Cs⁻, ZnC₂N₂⁻, C⁻ and In⁻ were also used as the markers for the layers here, too. CuI⁻ was added as the marker of the CuI

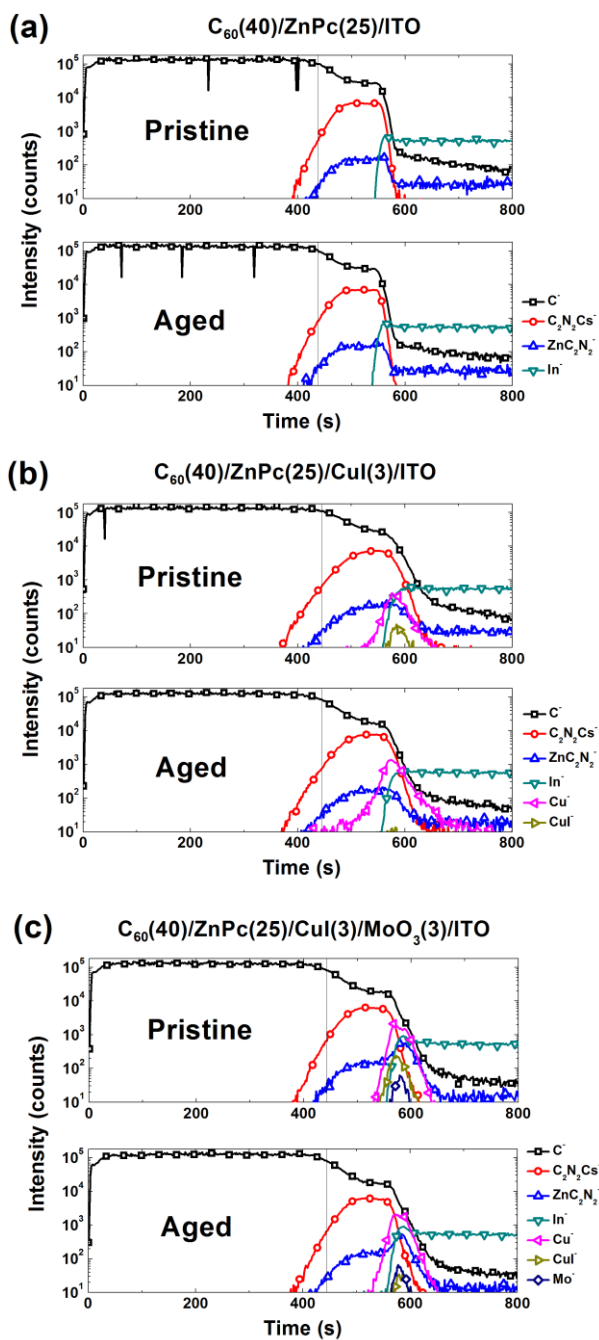


Figure 2.5 TOF-SIMS depth profiles of the samples in the negative mode with the structure of (a) ITO/ZnPc (25 nm)/ C_{60} (40 nm), (b) ITO/CuI (3 nm)/ZnPc (25 nm)/ C_{60} (40 nm), and (c) ITO/ MoO_3 (3 nm)/CuI (3 nm)/ZnPc (25 nm)/ C_{60} (40 nm).

layer in addition to the previous markers for the rest of the layers. CuI^- was observed at the interface between the ZnPc and ITO layers, as well as the mass spectrum of Cu^- , which is a fragment of CuI. 30 minutes illumination of UV light to the sample resulted in significantly different depth profiles from the pristine sample. The intensity of the CuI^- is reduced to almost zero and the intensity of Cu^- becomes higher and broadened. The spectral tail of the Cu^- moves to the interface between C_{60} and ZnPc, revealing that the Cu atoms or ions diffuse into the ZnPc layer to reach the interface of C_{60} and ZnPc. The photo-induced diffusion of Cu forms another path for charge transport separated from the *p-n* junction diode resulting in the reduction of the shunt resistance of the device. Prolonged illumination eventually leads to the loss of diode characteristics due to the reduced shunt resistance. These observations in the depth profiles are consistent with the photo-degradation characteristics of the device containing the CuI layer. The detailed mechanism of the diffusion of the Cu atoms or ions is not known yet. We could not find the evidence of the formation of Cu_2O , CuO or I_2 by UV irradiation in the TOF-SIMS data, indicating that the decomposition of CuI to elemental Cu and I_2 by the UV irradiation, or the reaction of the CuI with oxygen released from ITO under UV irradiation may not be origin of the Cu^- diffusion. In contrast, these phenomena were not observed in the depth profiles of the 3-nm-thick MoO_3 /3-nm-thick CuI double layer containing sample (Figure 2.5c). The Cu^- depth profile is

maintained without any change in shape after irradiation by UV light for 30 minutes by inserting the MoO₃ layer between the ITO and CuI layers. This fact suggests that the diffusion of Cu atoms or ions under UV light is prevented by insertion of the MoO₃ layer. Insertion of MoO₃ induces the formation of Cu₂O, I₂ and CuMoO_x complexes and prevents the diffusion of Cu atoms or ions (Figure 2.6). CuI still remains under UV illumination. This explanation is consistent with the significantly improved stability of the device under the illumination of light by the insertion of the MoO₃/CuI interfacial layer.

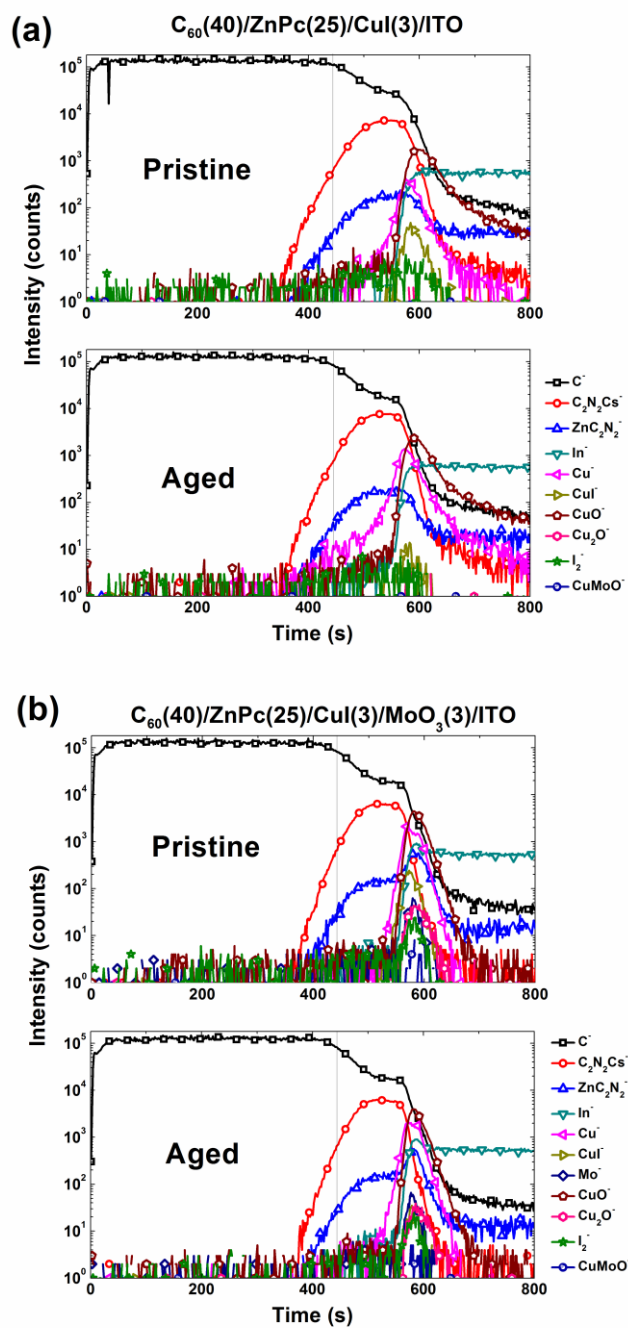


Figure 2.6 TOF-SIMS depth profiles of the samples in the negative mode with the structure of (a) ITO/CuI (3 nm)/ZnPc (25 nm)/ C_{60} (40 nm), and (b) ITO/ MoO_3 (3 nm)/CuI (3 nm)/ZnPc (25 nm)/ C_{60} (40 nm).

2.4 Conclusion

In summary, high efficiency and high photo-stability planar heterojunction solar cells were realized by inserting the CuI and MoO₃ double interfacial layer between the ITO and ZnPc layers. By using a CuI layer, the absorption coefficient of the ZnPc layer was improved and it led to a value of $\eta_p \sim 3\%$. However, the device with a CuI template layer showed a serious problem regarding photo-stability. In contrast, the device with a MoO₃/CuI double interfacial layer showed a much higher stability under illumination and did not show any degradation in the measured range. The TOF-SIMS analysis revealed that the diffusion of Cu atoms or ions is the origin of the photo-degradation of the device. Insertion of the MoO₃ layer between the ITO and CuI induces the formation of Cu₂O, I₂ and CuMoO_x complexes and prevents the diffusion of Cu atoms or ions under UV illumination. Our results indicate that the selection of materials for anode engineering and the combination of interfacial layers are important to improve the efficiency and stability of the planar heterojunction solar cells.

Chapter 3

The epitaxial growth of lead phthalocyanine on copper halogen compounds as the origin of templating effects

3.1 Introduction

The control of the crystal structure and the orientation of the molecules is an important research topic in organic electronics such as organic photovoltaics (OPVs) and organic thin film transistors (OTFTs) because the optical and electrical properties of the films strongly depend on them. One of the methods to control the crystal structure of molecules is to use a templating layer. The organic templating layers such as 3,4,9,10-perylenetetracarboxylic dianhydride (PTCDA), 2,5-bis(4-biphenyl)-bithiophene (BP2T), oxovanadium phthalocyanine (VOPc), sexithiophene (6T), para-sexiphenylene (*p*-6P), diindenoperylene (DIP) and pentacene have been used to control the crystal structure and/or the crystallinity of organic donor materials such as metal phthalocyanines.³⁻¹¹ Recently, CuI has been introduced as an effective templating material to control the crystal structure or the molecular orientation of copper phthalocyanine, zinc phthalocyanine and lead phthalocyanine (PbPc) molecules.¹²⁻²¹ The OPVs

showed nearly 2 times enhancement in a power conversion efficiency (η_p) by inserting the CuI templating layer. However, there are few reports on the mechanism of the templating effect of the CuI layer and it is not clearly understood yet.

In this work, we report that the templating effects originate from the epitaxial growth of organic molecules. CuCl, CuBr and CuI possessing different lattice spacings were selected as the templating layers. In addition, the PbPc was used as the organic donor material to analyse the templating effect because the increase of the crystallinity of PbPc film is easily noticed from change in absorption peaks at the wavelength of 740 nm and 900 nm which are related to the amorphous or the monoclinic phases and the triclinic phases.^{16,21,76} The dimensionless potentials between the copper halogen compound substrates and the PbPc overlayer calculated using a lattice model showed that the degree of epitaxy increases in the sequence of CuCl, CuBr and CuI, consistent with the experimental results of the crystallinity and absorption of the PbPc films on the templating layers and the resulting device performance.

3.2 Experimental

3.2.1 Device fabrication and characterization

The control device had the following planar heterojunction structure: indium tin oxide (ITO) (150 nm)/ PbPc (20 nm)/ C₆₀ (40 nm)/ BCP (8 nm)/ Al (100 nm). The ITO-coated glass substrate was successively cleaned with acetone and isopropyl alcohol. The substrate was exposed to UV-O₃ for 10 min before use. All the organic layers were deposited using thermal evaporation at the base pressure of ca. 10⁻⁷ torr with a rate of 1 Å/s without breaking the vacuum. CuCl, CuBr and CuI layers were also thermally deposited onto the substrate with a rate of 0.2 Å/s. The devices had active areas of 2×2 mm². A patterned insulator on the ITO and the top cathode deposited through a shadow mask defined the cell area. After fabrication, the devices were encapsulated using an epoxy resin with glass cans in an N₂ environment. More than 8 cells for each device structure were fabricated and the mean values of the photovoltaic performances and standard deviations were obtained. The photovoltaic properties of the devices were measured with an AM 1.5G 100 mWcm⁻² solar simulator (300 W Oriel 69911A) light source and a source measurement unit (Keithley 237). The measurement set up was calibrated with a National Renewable Energy Laboratory-certified reference Si-solar cell covered with a KG-5 filter

before every measurement.

3.2.2 Characterization of thin films

The UV–vis absorption spectra of films were recorded with a VARIAN Cary 5000 UV–vis spectrophotometer. The crystalline structures were investigated by synchrotron x-ray diffraction measurements at 5A x-ray scattering beamline for materials science of Pohang Light Source II (PLS-II). The x-ray wavelength was 1.071 Å (11.58 KeV). The films were deposited on ITO substrates. Atomic force microscope (AFM) topographic images of the films were taken using a PSIA XE-100 scanning probe microscope in the non-contact mode.

3.3 Result and discussion

3.3.1 Optical and structural analyses of lead phthalocyanine films on various copper halogen compounds layer

The templating effect of the copper halogen compounds on the absorption of the PbPc films is shown in Figure 3.1. The 20 nm-thick PbPc film was deposited on 3 nm-thick CuCl, CuBr and CuI coated ITO substrates. The intensity of the absorption peak at the wavelength of 740 nm in the Q-band absorption of PbPc is gradually reduced in the order of CuCl, CuBr and CuI and the peak at 900 nm is newly developed in the same order resulting in the two times enhancement by inserting the CuI layer. The broadened Q-band absorption of the PbPc film can be assigned as the increase of the monoclinic phase in the film.¹⁶ The grazing incident angle x-ray diffraction (GIXD) was performed with the incident angle of 0.2° to investigate the crystalline property of the PbPc films and the GIXD patterns of the samples are depicted in Figure 3.2(a). The pristine 20 nm-thick PbPc film on ITO without the templating layers shows the diffraction peaks at $Q = 8.89 \text{ nm}^{-1}$ and $Q = 11.72 \text{ nm}^{-1}$ which are assigned as the (320) plane of the monoclinic PbPc phase and $(1 \bar{3} 0)$ plane of the triclinic phase, respectively.^{16,76} The diffraction peak of the $(1 \bar{2} 1)$ plane of the triclinic phase is shown at $Q = 9.15 \text{ nm}^{-1}$.⁷⁶ The intensity of the diffraction peak of

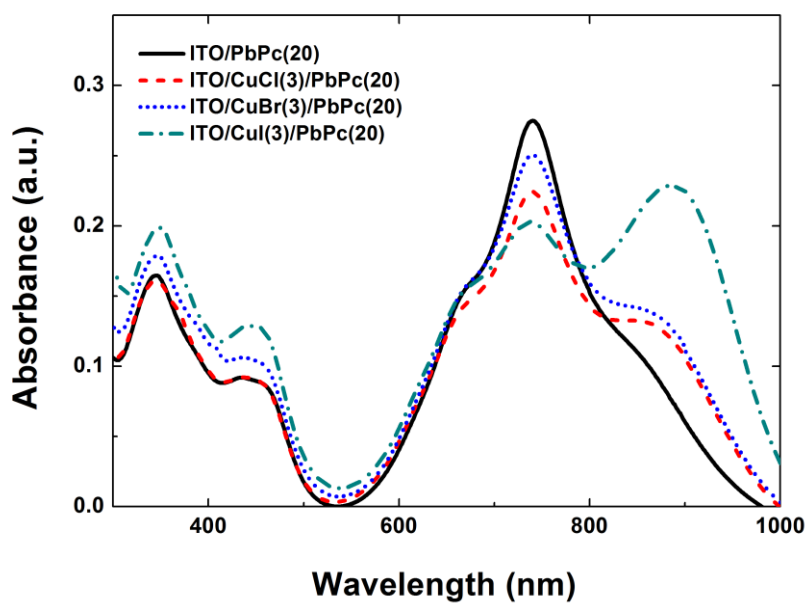


Figure 3.1 The absorption spectra of pristine 20 nm-thick PbPc film grown on ITO (black line) and films grown on 3 nm-thick CuCl (red dashed line), CuBr (blue dot line) and CuI (green dashed dot line) deposited on the ITO substrates, respectively.

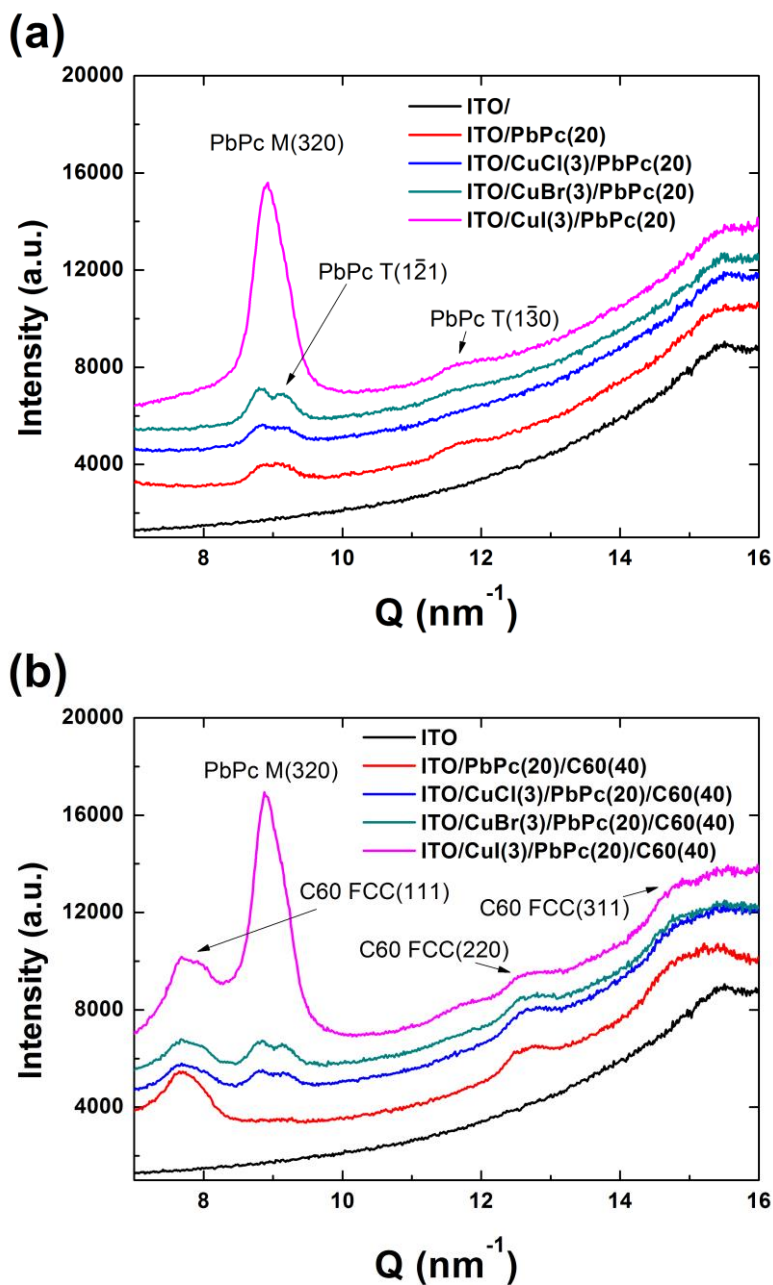


Figure 3.2 (a) The X-ray diffraction patterns of ITO (black), PbPc (20 nm) (red), CuCl (3 nm)/PbPc (20 nm) (blue), CuBr (3 nm)/PbPc (20 nm) (green) and CuI (3 nm)/PbPc (20 nm) (pink) deposited on the ITO pre-coated glass. (b) The X-ray diffraction patterns of the films after the deposition of C₆₀ layer on top of the PbPc layer.

the (320) plane of the monoclinic PbPc phase gradually increased in the order of CuCl, CuBr and CuI, which is the same tendency as the broadening of the Q-band absorption peak.

The diffraction patterns of the same samples after the deposition of a 40 nm-thick of C₆₀ layer on top of the PbPc layers are shown in Figure 3.2(b). The diffraction peaks at $Q = 7.69 \text{ nm}^{-1}$, $Q = 12.64 \text{ nm}^{-1}$ and $Q = 14.87 \text{ nm}^{-1}$ are assigned as the (111) plane, (220) plane and (311) plane of the face centered cubic (FCC) phase of C₆₀.⁷⁷ The diffraction peaks of (320) plane of the monoclinic PbPc phase and $(1\bar{2}1)$ plane of the triclinic PbPc phase disappeared after the deposition of the C₆₀ layer, indicating that the crystal structure is demolished by the deposition of the C₆₀ molecules due to the interaction with C₆₀ at the interface or the diffusion of C₆₀ molecules into the organic layer. It can take place because large portion of the PbPc crystalline is located near the surface, exhibiting the thickness dependent phase transition.⁷⁶ However, the diffraction peaks of PbPc grown on the copper halogen compounds are retained after the deposition of C₆₀ layer, indicating that the crystalline PbPc in the film grown on the copper halogen compounds is less affected by the deposition of C₆₀ layer because it locates near the interface of the copper halogen compounds/PbPc or distributed in the whole layer.

3.3.2 Lattice modelling by energetic consideration

The templating effect was analysed based on the concept of heteroepitaxy where the molecule-substrate bonding due to electrostatic interactions between the molecules and the anion in the ionic compounds is considered as the driving force to control the crystal structure and the molecular orientation of the organic molecules.^{37,78,79} The dimensionless potential V/V_0 has been calculated by a simple analytic method to evaluate the heteroepitaxial system by considering the geometrical lattice mismatch.⁸⁰ This approach can analyse the phase coherence between an overlayer and substrate unit cells and describe their potential energy as simple plane waves which is modelled by cosine functions. The value of V/V_0 is determined by the degree of epitaxy between overlayer and substrate in the range $-0.5 < V/V_0 < 1$ where $V/V_0 = 1$ for incommensurism, $V/V_0 = 0.5$ for coincidence, $V/V_0 = 0$, $V/V_0 = -0.5$ for commensurism on a nonhexagonal and hexagonal substrates, respectively. First of all, we calculated the potential energy of the PbPc 55×55 overlayer on the series of copper halogen compounds with the lattice parameters ranging from 1 to 14 Å with 0.001 Å of grid. The copper halogen compounds have the zinc blende (111) structure on ITO substrates as shown in Figure 3.3 and PbPc molecules are assumed to be grown with the monoclinic (320) structure dominantly on the copper halogen compounds.⁸ The lattice parameters of the PbPc monoclinic phase and the copper halogen compounds used for the calculation are summarized in Table 3.1, which were taken from literature.^{16,76,81-86} The schematic representation of the overlayer of PbPc

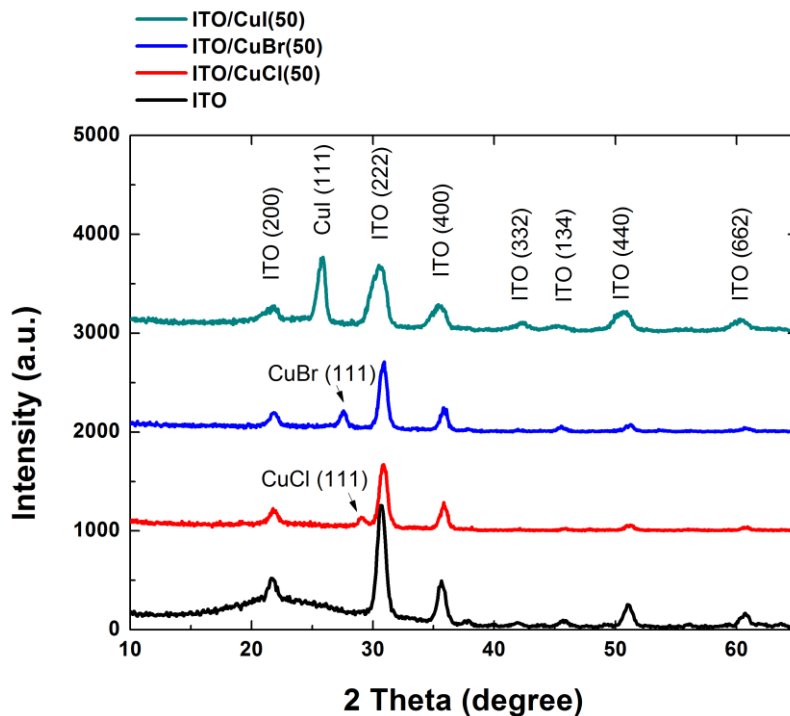


Figure 3.3 The X-ray diffraction profiles of ITO (black), ITO/CuCl (50 nm) (red), ITO/CuBr (50 nm) (blue), ITO/CuI (50 nm) (green)

Table 3.1 The lattice parameters of PbPc monoclinic and copper halogen compounds with zinc blende structure.

	a [Å]	b [Å]	c [Å]	$\alpha=\beta=\gamma$ [°]
PbPc	25.48	25.48	3.73	90
CuCl	5.424	5.424	5.424	90
CuBr	5.695	5.695	5.695	90
CuI	6.054	6.054	6.054	90

monoclinic (320) and zinc blende (111) ionic compounds substrate are displayed and the seven parameters a_1 , a_2 , α' and b_1 , b_2 , β' for representing the unit cells and the azimuthal angle θ between the overlayer and the substrate unit cells used in the calculations are defined in Figure. 3.4(a). The dependences of the potential V/V_0 on azimuthal angle θ of PbPc 55×55 overlayer and CuCl, CuBr and CuI substrates used in our works are presented in Figure 3.4(b). The calculation results predict the degree of epitaxy at specific angles. The minima of potential V/V_0 when using CuCl and CuBr show values of 0.81, 0.74, respectively. CuI showed the smallest potential V/V_0 value of 0.63 at θ of 2.3° among them, indicating that the PbPc monoclinic phase with the (320) orientation forms the coincidence epitaxy most favourably using CuI as the templating layer. The analysis predicts that the larger monoclinic crystals with better crystallinity are formed using the CuI templating layer followed by CuBr and CuCl, which are in good agreement with the experimental results. The consistency between the experimental results and the theoretical analysis suggests that the templating effects originate from the heteroepitaxial growth of the PbPc films on the copper halogen compounds. Furthermore, the crystal structure of the organic thin film is closely related with the lattice parameters of the ionic compounds. In other words, the organic thin film is grown toward minimizing the strain energy between the molecule-substrate lattice mismatch. Growth of organic molecules on ionic compounds such as KBr, KCl and NaCl was previously explained by a heteroepitaxy.^{38,39,80}

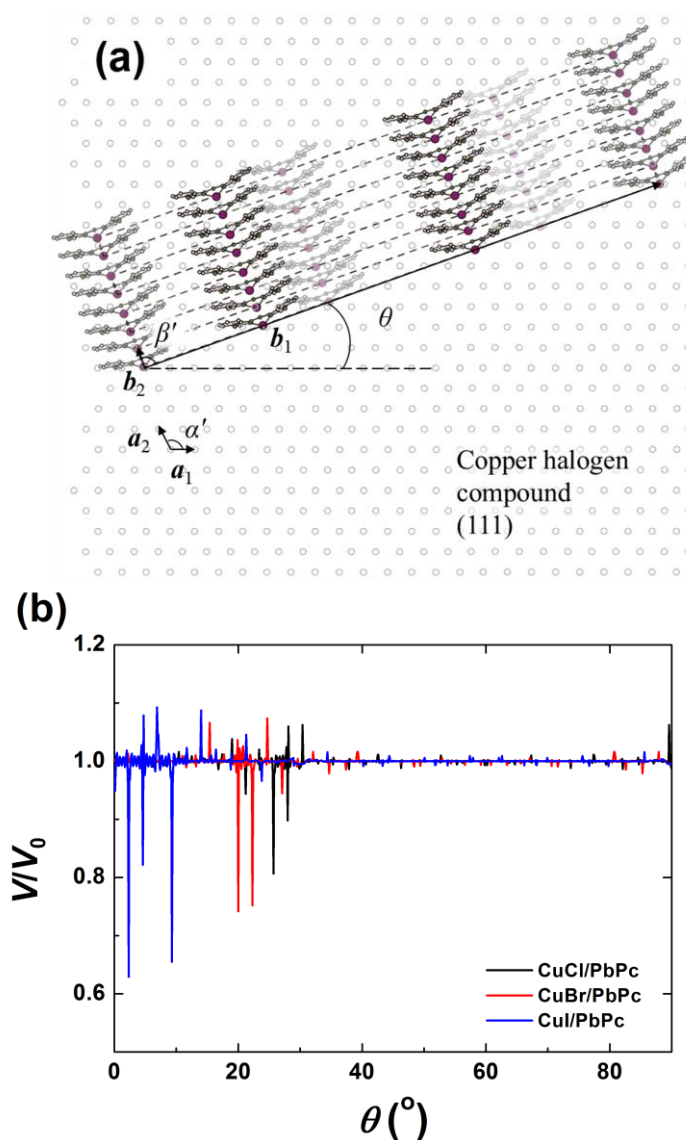


Figure 3.4 (a) Schematic representation of PbPc monoclinic (320) overlayers on copper halogen compounds. The parameters a_1 , a_2 and α' of the substrates and b_1 , b_2 and β' of the PbPc layer were calculated from the lattice parameters of the respective unit cells. The azimuthal angle θ represents the angle between the vector a_1 and b_1 . (b) Calculated V/V_0 against azimuthal angle θ of PbPc overlayer on CuCl (black line), CuBr (red line) and CuI (blue line), respectively.

3.3.3 Investigation of surface morphology

The AFM images in Figure 3.5 illustrate the variation of the surface morphology of the 5 nm-thick PbPc films on the different copper halogen compounds substrates. The initial growth of the several monolayer of PbPc molecules shows the Stranski-Krastanov (SK) mode on the CuI substrate and the Volmer-Weber (VW) mode on pristine ITO substrate due to the increase of the lattice mismatch.⁸⁷ The surface coverage is the largest on the CuI substrate and larger island of the PbPc with small coverage are formed on the pristine ITO substrate. The coverage of the PbPc films becomes larger with increase of the thickness of PbPc films.

3.3.4 Photovoltaic characteristics of devices

The templating effects are manifested in the performance of the OPVs. The current density-voltage (J - V) characteristics of the devices formed on different templating layers are represented in Figure 3.6(a). The photovoltaic parameters, the parallel resistance (R_p) and the series resistance (R_s) extracted from the dark J - V curves with the equivalent Shockley diode equation are summarized in Table 3.2. The control device showed the η_p of 1.53% with the short-circuit current density (J_{SC}) of 5.26 mAcm^{-2} , the open-circuit voltage (V_{OC}) of 0.52 V and the fill factor (FF) of 0.57. Insertion of the CuCl, CuBr and CuI templating layers enhanced J_{SC} to 7.67, 7.60, 7.89

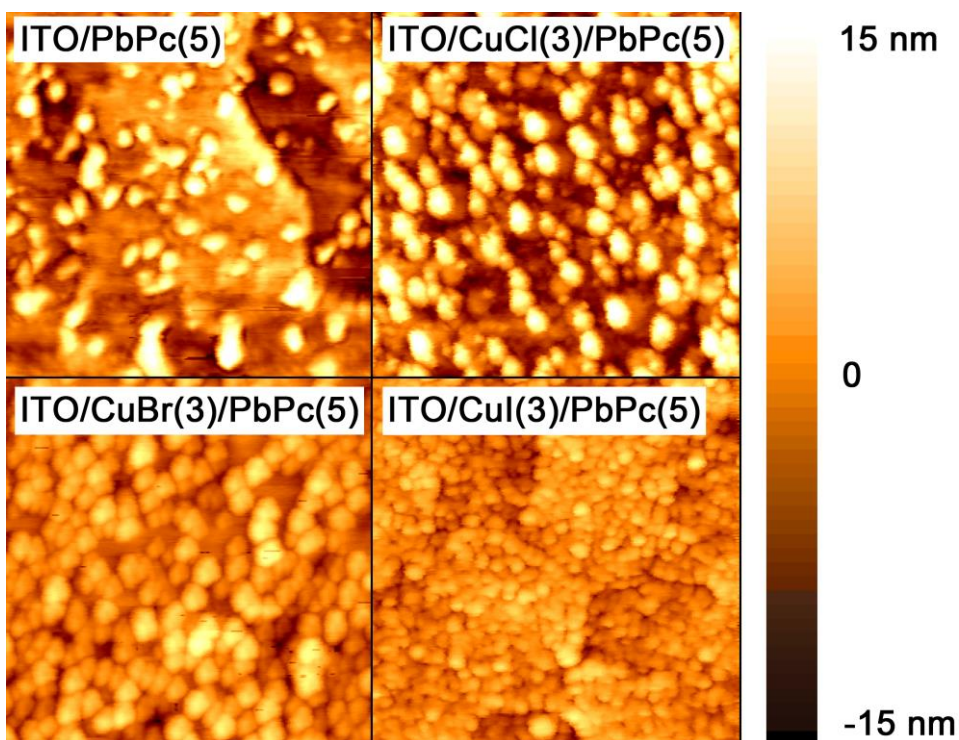


Figure 3.5 AFM images of the 5 nm-thick PbPc film grown on the ITO and 3 nm-thick CuCl, CuBr and CuI coated ITO substrate are displayed, respectively. The images are $1 \times 1 \mu\text{m}^2$

mAcm^{-2} , thereby, the η_p to 1.82, 1.97, 2.10%, respectively. The lower FF of the device with CuCl is reflected in higher R_s of $13.84 \Omega\text{cm}^2$, which might be related to its deep valence band energy level (CuCl; 6.9 eV, CuBr; 5.6 eV, CuI; 5.0 eV) working as a potential barrier for hole-transport at the interface between ITO and active layer.⁸¹ The increase of J_{SC} originates from the enhancement of incident photon-to-current efficiency (IPCE) in the part of PbPc molecules (Figure 3.6(b)). In our previous work, the exciton diffusion length (L_D) increased with enhancement of crystallinity by insertion of the templating layer.¹³ The GIXD results in Figure 3.2(b) indicate that the copper halogen compounds prevent the PbPc film from losing the crystallinity after the deposition of C_{60} and it is the origin of higher L_D and IPCE of the devices with the copper halogen compounds. In addition, decrease of V_{OC} from 0.52 V to 0.47, 0.47, 0.45 V can be explained by the reduced band gap of the PbPc film due to the intermolecular interaction of molecules, manifested in the red-shifted absorption spectra of PbPc films and IPCE spectra of the devices with the copper halogen compounds. Since V_{OC} of OPVs is related with the energy level difference between the lowest unoccupied molecular orbital (LUMO) level of acceptor and the highest occupied molecular orbital (HOMO) level of donor material, the change in V_{OC} can be explained by the shift of energy level of PbPc film.

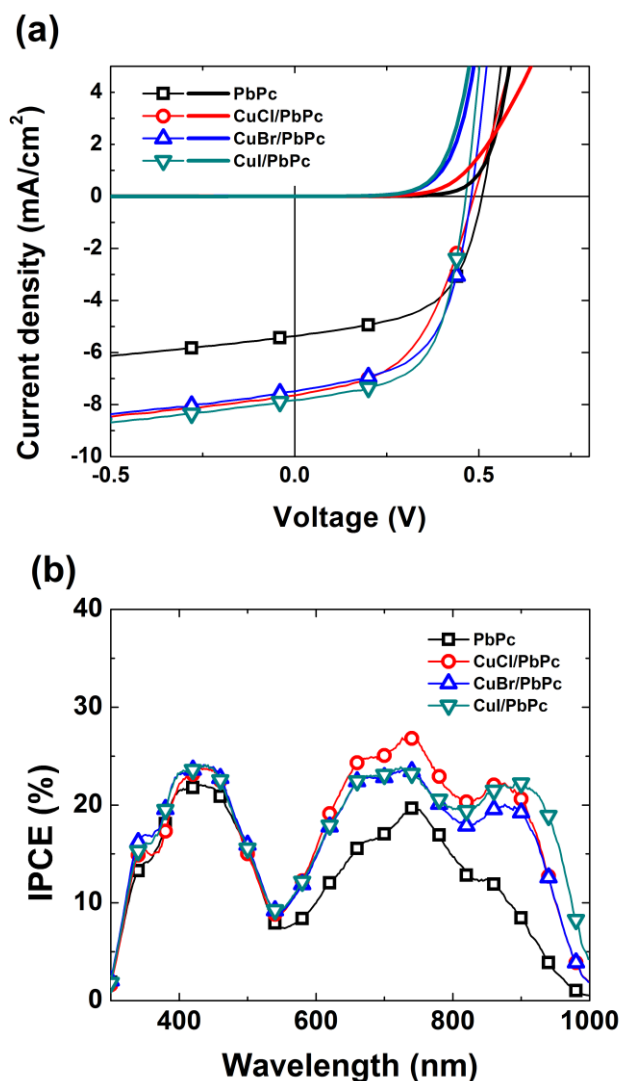


Figure 3.5 (a) The J - V characteristics of the OPVs with the copper halogen compounds. The control device (black square) is comprised of ITO/PbPc (20 nm)/C₆₀ (40 nm)/BCP (8 nm)/Al. The devices with a 3 nm-thick CuCl (red circle) layer, 3 nm-thick CuBr (blue triangle) and 3 nm-thick CuI (green triangle) inserted between the ITO and PbPc layers in the control device are also shown. (b) The IPCE spectra of the PbPc based control device (black square) and devices with CuCl (red circle), CuBr (blue triangle) and CuI (green triangle) are displayed.

Table 3.2 The summary of photovoltaic parameters and R_P , R_S extracted from dark J - V curves by using Shockley equation of the devices with copper halogen compounds.

	PbPc	CuCl/PbPc	CuBr/PbPc	CuI/PbPc
η_p [%]	1.53±0.013	1.82±0.056	1.97±0.101	2.10±0.056
J_{SC} [mAcm ⁻²]	5.26±0.086	7.67±0.103	7.60±0.093	7.89±0.064
V_{oc} [V]	0.52±0.016	0.47±0.016	0.47±0.008	0.45±0.011
FF	0.57±0.013	0.51±0.012	0.55±0.036	0.59±0.010
R_P [×10 ⁶ Ωcm ²]	5.07	0.11	0.15	0.12
R_S [Ωcm ²]	3.07	13.84	3.33	4.59

3.4 Conclusion

We have investigated the templating effect of copper halogen compounds on PbPc films using the theory of heteroepitaxy. Simple lattice modelling predicted that the PbPc monoclinic phase with the (320) orientation forms the coincidence epitaxy most favourably using CuI as the templating layer minimizing the potential energy due to the least lattice mismatch between the organic crystal and templating layer followed by CuBr and CuCl. The change of phase and the enhancement in crystallinity of the PbPc film on the copper halogen compounds are consistent with our calculation; more pronounced formation of the PbPc monoclinic phase with the (320) orientation and enhanced crystallinity in the sequence of CuI>CuBr>CuCl. In addition, the initial growth modes of the PbPc films are influenced by the degree of the lattice mismatch between the organic crystal and templating layer. Large mismatch (PbPc on ITO) resulted in the island (VW) growth mode with low surface coverage but small mismatch (PbPc on CuI) resulted in the SK growth mode with much better surface coverage. Apparently the different growth modes on different templates influence the performance of the PbPc based OPV; the templating layer with less lattice mismatch resulted in higher η_p s in the sequence of CuI>CuBr>CuCl>none on ITO. We believe that the application of the concept of heteroepitaxy is not limited to our specific system but can be a general phenomenon in

organic/organic and organic/inorganic multilayer systems and the degree of the heteroepitaxy depends on the interaction energy between the templating layer and the overlayer. This heteroepitaxy must have the important application not only in OPVs and OTFTs but also in every area where organic crystalline structure plays importance roles.

Chapter 4

Multilayer epitaxial growth of lead phthalocyanine and C₇₀ using CuBr as a templating layer for enhancing the efficiency of organic photovoltaic cells

4.1 Introduction

Tremendous progress has been made in small molecule based organic photovoltaic cells (OPVs) in recent years, demonstrating a power conversion efficiency (η_p) up to ~8.9% using the solution process,^{57,88-90} and ~8.1% using the vacuum process.^{58,91-93} For the next leap, many researchers are paying attention to the control of the crystal structure and orientation of the molecules because the optical and electrical characteristics of organic films are strongly connected with the crystal structure. The use of templating layers has been considered to be an effective way to control the crystal structure and molecular orientation by using intramolecular interactions.⁵⁻⁸ The molecule-substrate bonding resulting from the electrostatic interactions between molecules and anions in ionic compounds is known to be the driving force to control the crystal structure and to form the preferred orientation of organic molecules.^{4,37,78,80} Recently, CuI has been successfully used as a templating material to achieve significant

enhancement of η_p with classical donor materials.^{12-17,19,21} However, until now, templating effects have been confined on donor materials deposited on the templating layer. A way to control the phase of the acceptor materials deposited on the donor materials is needed for higher efficiency OPVs.

Here, we demonstrate a multilayer epitaxy by employing CuBr as a templating layer and lead phthalocyanine (PbPc) and C₇₀ as the donor and acceptor molecules, respectively. PbPc formed the monoclinic phase with a (320) preferred orientation on CuBr and the Q-band absorption located in the near-IR region of the molecules is developed by the templating effects.²¹ In addition to that, C₇₀ formed the face-center-cubic (fcc) phase with the preferred orientation of (220) when deposited on the crystalline PbPc grown on the CuBr templating layer. The multilayer epitaxy results in the increase of the exciton diffusion lengths (L_D) and the absorption in both layers to enhance the η_p of the planar heterojunction OPVs composed of PbPc and C₇₀ from 1.4 to 2.3%.

4.2 Experimental

4.2.1 Device fabrication and characterization

The organic solar cells used in this study have the following structure: ITO/PbPc (20 nm)/C₇₀ (50 nm)/bathocuproine (BCP) (8 nm)/Al (100 nm) with and without a 3 nm thick CuBr layer between the ITO and PbPc layers to investigate the templating effect. The ITO-coated glass substrate was successively cleaned with acetone and isopropyl alcohol and the substrate was exposed to UV-O₃ for 10 min before use. All of the organic layers were deposited using thermal evaporation at a base pressure of ca. 10⁻⁷ torr with a rate of 1 Å/s. The CuBr layer was also deposited using thermal evaporation onto the substrate at a rate of 0.2 Å/s. The aluminum metal cathode was deposited with a rate of 4 Å/s. All the layers were successively evaporated without breaking the vacuum. The devices had active areas of 2×2 mm². A patterned insulator on the ITO and the top cathode deposited through a shadow mask defined the cell area. After fabrication, the devices were encapsulated using epoxy resin with glass cans under an N₂ environment. The photovoltaic properties of the devices were measured with an AM 1.5G 100 mW cm⁻² solar simulator (300 W Oriel 69911A) light source and a source measurement unit (Keithley 237). The measurement setup was calibrated with a National Renewable Energy Laboratory-certified reference

Si-solar cell covered with a KG-5 filter before every measurement. More than 8 cells for each device structure were fabricated and the mean values of the photovoltaic performances and standard deviations were obtained.

4.2.2 Characterization of thin films

The UV-vis absorption spectra of films were recorded with a VARIAN Cary 5000 UV-vis spectrophotometer. The films were thermally evaporated on UV-O₃ treated ITO substrates. The crystalline structures were investigated by synchrotron x-ray diffraction measurements at 5A x-ray scattering beamline for materials science of Pohang Light Source II (PLS-II). The x-ray wavelength was 1.071 Å (11.58 KeV) at an incident angle of 0.1°.

4.3 Result and discussion

4.3.1 Photovoltaic characteristics of devices

Figure 4.1 shows the current density-voltage (J - V) characteristics of the devices measured under light and dark conditions using the illumination of an AM 1.5G 100 mW cm⁻² solar-simulated light source. The photovoltaic parameters of the devices are summarized in Table 4.1. J_{SC} was mainly increased by the insertion of CuBr from 5.53 mA cm⁻² to 9.44 mA cm⁻² and the fill factor (FF) was also increased from 0.49 to 0.52. As a result, PCE showed considerable enhancement over 1.6 times from 1.45 to 2.34% with the insertion of the CuBr layer despite the slightly reduced open-circuit voltage (V_{OC}) from 0.53 to 0.48. The origin of the reduction of V_{OC} is not clear yet, but it can be discussed on the basis of the variation of the diode parameters in the devices. V_{OC} in the Shockley diode equation can be expressed as follows⁹⁴

$$V_{OC} = \frac{nkT}{q} \ln\left(\frac{J_{SC}}{J_S}\right) \quad (1)$$

where n is the ideality factor, k is the Boltzmann constant, q is the elementary charge, and J_S value is the dark saturation current density. The diode parameters are extracted from the dark J - V characteristic curves and displayed in Table 4.1. The J_S increases from 1.57×10^{-4} to 3.05×10^{-4}

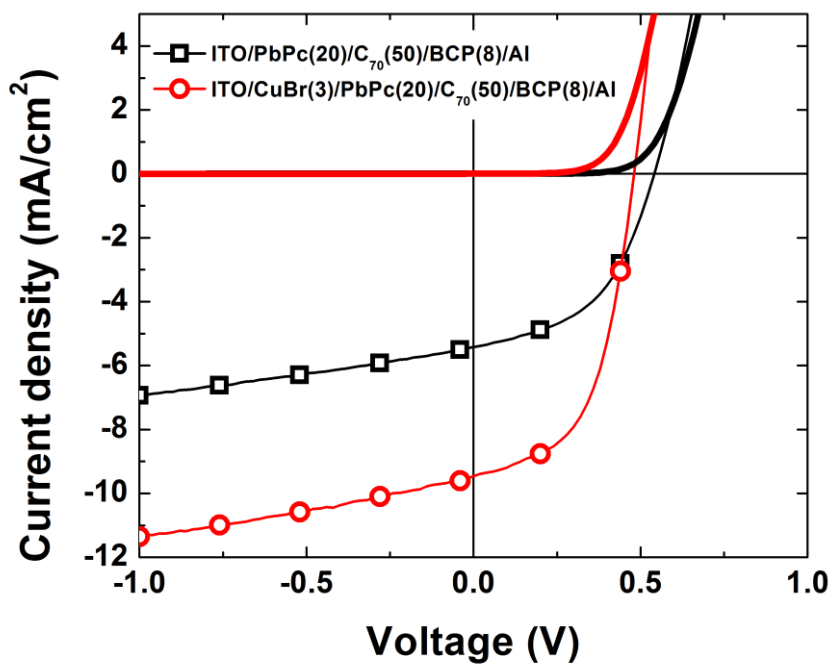


Figure 4.1 The J - V characteristics the OPVs with and without the CuBr layer. The control device (black square) is comprised of ITO/PbPc (20 nm)/C₇₀ (50 nm)/BCP (8 nm)/Al. The device with a 3 nm-thick CuBr (red circle) layer inserted between the ITO and PbPc layers in the control device is shown.

Table 4.1 The photovoltaic parameters of the solar cells under AM 1.5G 1 sun illumination. The J_s , R_P and R_S values are extracted from dark J - V curves by using the Schokley diode equation.

	ITO/PbPc(20)/ C ₇₀ (50)/BCP(8)/Al	ITO/CuBr(3)/PbPc(20)/ C ₇₀ (50)/BCP(8)/Al
η_p [%]	1.45±0.02	2.34±0.10
J_{sc} [mA/cm ²]	5.53±0.08	9.44±0.17
V_{oc} [V]	0.53±0.02	0.48±0.01
FF	0.49±0.01	0.52±0.03
R_P [Ωcm^2]	6.47×10 ⁶	2.41×10 ⁵
R_S [Ωcm^2]	6.64	9.01
n	2.41	1.98
J_s [mA/cm ²]	1.57×10 ⁻⁴	3.05×10 ⁻⁴
Calculated V_{oc} [V]	0.65	0.53

mA/cm^2 and n decreases from 2.41 to 1.98 when the CuBr templating layer is used. The calculated V_{OC} by using equation (1) are 0.53 V and 0.65 V with and without the CuBr templating layer, respectively, and this tendency is consistent with the change of the measured V_{OC} values of the devices with and without the CuBr layer. Because the J_{S} is a function of the difference between the highest occupied molecular orbital (HOMO) level of the donor and the lowest unoccupied molecular orbital (LUMO) level of the acceptor,⁹⁴ the change in the energy level alignment of the active layers with a CuBr templating layer is a possible origin of the reduction of V_{OC} . Different orientation and different phases have been reported to give different HOMO levels, resulting in different V_{OC} values.^{24,95}

4.3.2 Optical characterization of devices and extraction of exciton diffusion length by optical modelling

To understand the templating effect, the absorption spectra and the incident photon-to-current efficiency (IPCE) spectra of the ITO/PbPc (20 nm) and ITO/CuBr (3 nm)/PbPc (20 nm) films were measured and are shown in Figure 4.2 and Figure 4.3, respectively. The absorption peak at a wavelength of 900 nm in the Q-band absorption is more pronounced at the expense of the reduced absorption peak at 740 nm by the insertion of the CuBr layer. This change can be explained by the formation of the monoclinic phase with a (320) preferred orientation, indicating that the

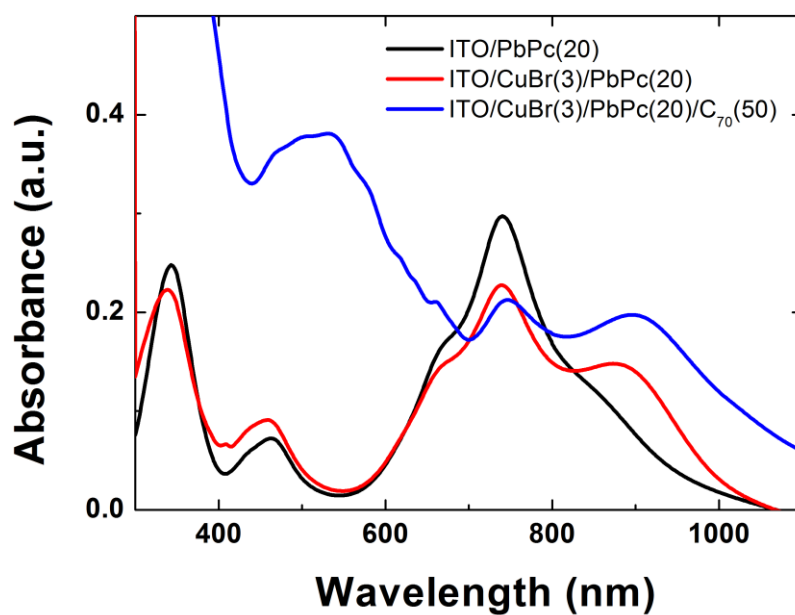


Figure 4.2 The absorbance spectra of the films with the structures of ITO/PbPc (20 nm), ITO/CuBr (3 nm)/PbPc (20 nm) and ITO/CuBr (3 nm)/PbPc (20 nm)/C₇₀ (50 nm) are represented by the black, red and blue lines, respectively.

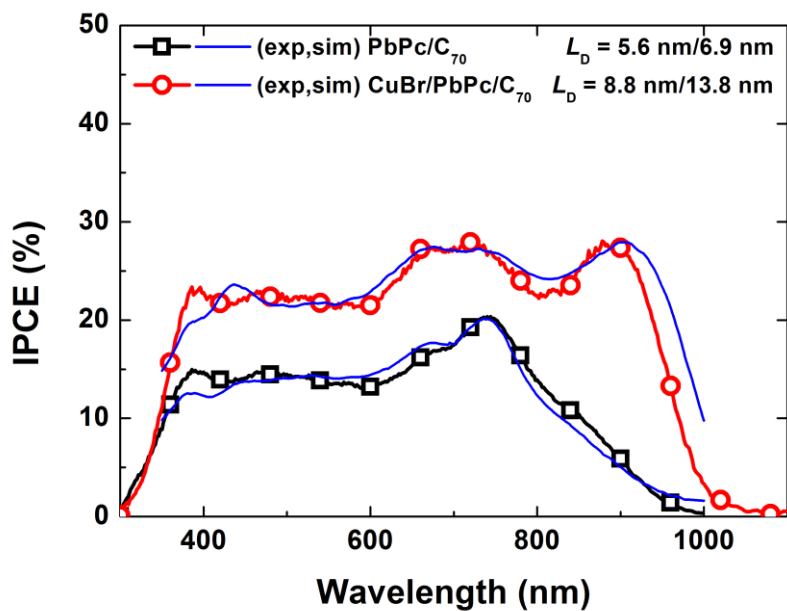


Figure 4.3 The measured IPCE spectra of the control device (black square) and the device with the CuBr (red circle) templating layer are displayed, and the simulated IPCE spectra using the L_D values shown in the legend are also displayed by the blue lines.

CuBr layer acts as a templating layer for the PbPc molecules to enhance the crystallinity of the PbPc film.¹⁶ The IPCE spectrum of the device with the CuBr layer is also broadened in the Q-band region. However, the ratio of the peak intensities at 740 nm and 900 nm in the IPCE spectrum of the device with CuBr is different from the ratio in the absorption spectrum of the ITO/CuBr (3 nm)/PbPc (20 nm) film. The optical simulation of the devices showed that the difference did not originate from an optical interference effect resulting from stacking additional C₇₀, BCP and Al layers. The difference can instead be understood from the absorption spectrum of the ITO/CuBr (3 nm)/PbPc (20 nm)/C₇₀ (50 nm) film, as shown in Figure 4.2. Surprisingly enough, the absorption peak at a wavelength of 900 nm is more broadened and the absorption intensity is also increased after the deposition of C₇₀ onto the PbPc layer. In contrast, the absorption peak at a wavelength of 740 nm is reduced again after the deposition of C₇₀. The ratio of the two absorption peak intensities is now in very good agreement with the IPCE spectrum. This result strongly suggests that the PbPc molecules near the surface are rearranged after the deposition of C₇₀ onto the PbPc layer. In addition to the modification of the PbPc absorption, the IPCE was also improved in the absorption region of C₇₀ by inserting the CuBr layer, implying that the monoclinic phase of the PbPc layer formed by the CuBr interlayer acts as a templating layer for C₇₀. To the best of our knowledge, this is the first time an organic multilayer epitaxy with both donors and acceptors in OPVs using a templating layer has been reported. This effect

was not observed in the device based on C₆₀. Even though the J_s was increased significantly in the C₆₀ based device by inserting the CuBr layer, the IPCE coming from the C₆₀ absorption did not change much (Figure 4.4). The difference in the lattice constants of the bulk crystal of C₆₀ and C₇₀ is a possible origin of the different behaviors. The lattice matching condition between the monoclinic phase of PbPc and the fcc and hexagonal close-packed (HCP) phases of C₆₀ was not found from the calculation of dimensionless potential, indicating that quasi epitaxial growth is not allowed between PbPc and C₆₀.

The formation of the crystals in the PbPc and C₇₀ layers resulted in the increase of the L_D values in the layers increasing the J_{SC} or IPCE. The L_D values in the organic layers were extracted from the fitting of the measured IPCEs using the transfer matrix method with the L_D values as the parameters.⁹⁶ For the extraction of L_D the refractive indices of the 60 and 20 nm-thick PbPc films grown on ITO were used for the ITO/CuBr/PbPc and ITO/PbPc films, respectively, because they have similar absorption spectra each other.⁷⁶ The fitting results in Figure 4.3 showed that the L_D value of the PbPc layer increased from 5.6 ± 0.08 nm to 8.8 ± 0.13 nm by inserting the CuBr layer, which is consistent with previous results.¹³ Moreover, the L_D value of the C₇₀ layer was improved by almost a factor of two, from 6.9 ± 0.10 nm to 13.8 ± 0.21 nm, also by the insertion of the CuBr layer. As a result, the J_{SC} value of the device increased by 1.7 times, from 5.53 mA cm^{-2} to 9.44 mA cm^{-2} .

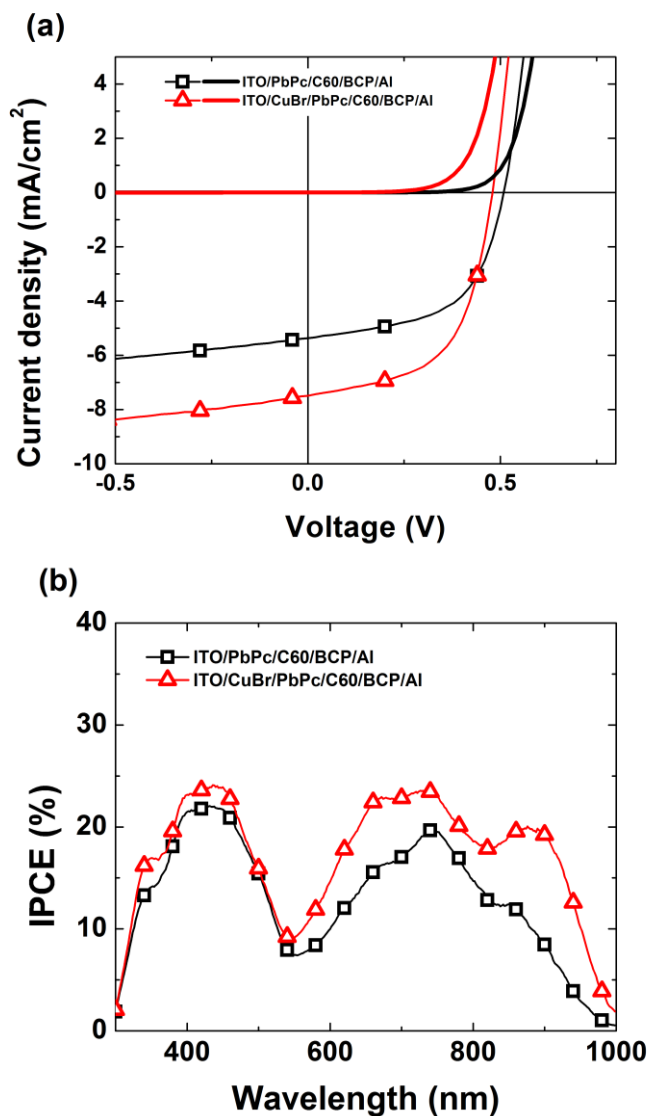


Figure 4.4 (a) J - V characteristic curves and (b) IPCE spectra of ITO/PbPc (20 nm)/C₆₀ (40 nm)/BCP (8 nm)/Al (black square) and ITO/CuBr (3 nm)/PbPc (20 nm)/C₆₀ (40 nm)/BCP (8 nm)/Al (red triangle).

4.3.3 Structural analysis by using X-ray spectroscopy

The structural change of the molecules was investigated using the x-ray diffraction (XRD) patterns shown in Figure 4.5a. The diffraction pattern of the 20 nm thick PbPc layer deposited on an ITO substrate showed two peaks near $Q = 9 \text{ nm}^{-1}$ and 11.67 nm^{-1} which can be assigned as the mixture of the (320) oriented monoclinic phase ($Q = 8.81 \text{ nm}^{-1}$), the $(1\bar{2}1)$ oriented triclinic phase ($Q = 9.12 \text{ nm}^{-1}$) and the $(1\bar{3}0)$ oriented triclinic phase ($Q = 11.67 \text{ nm}^{-1}$).^{16,76} When the PbPc was grown on the ITO/CuBr (3 nm) the crystallinity of the monoclinic phase and the $(1\bar{2}1)$ oriented triclinic phase was increased and the amount of the $(1\bar{3}0)$ oriented triclinic phase was reduced. However, the 50 nm-thick C_{70} layer deposited on ITO has a fcc structure with a (111) preferred orientation identified by the diffraction peak at $Q = 7.36 \text{ nm}^{-1}$. Interestingly, the intensity of the C_{70} peaks was intensified and the PbPc peaks disappeared when the C_{70} layer was grown on the ITO/PbPc layer. This fact indicates that the crystallinity of the underlying PbPc layer was demolished by the deposition of the C_{70} on top of PbPc, clearly demonstrating that the overlayer of C_{70} significantly modified the structure of the underlying layer. In contrast, the crystallinity of the PbPc layer grown on the ITO/CuBr remained with slight modification of the structure after the deposition of the C_{70} layer. Furthermore, the diffraction peak near $Q = 9 \text{ nm}^{-1}$ of the PbPc layer becomes stronger after the

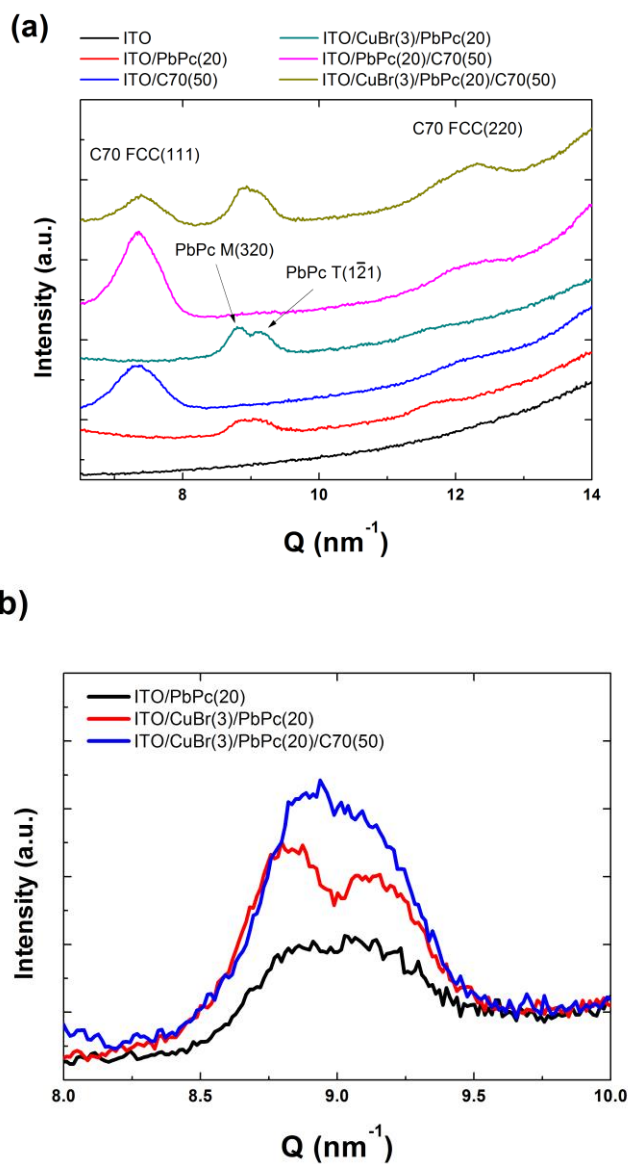


Figure 4.5 (a) XRD profiles of the films with the following structures: ITO/PbPc (20 nm), ITO/CuBr (3 nm)/PbPc (20 nm), ITO/C₇₀ (50 nm), ITO/PbPc (20 nm)/C₇₀ (50 nm), and ITO/CuBr (3nm)/PbPc (20 nm)/C₇₀ (50 nm). The peaks of monoclinic PbPc with a (320) orientation and FCC C₇₀ with (111) and (220) orientations are also displayed. (b) The comparison of the peaks of the films ITO/PbPc (20 nm), ITO/CuBr (3 nm)/PbPc (20 nm) and ITO/CuBr (3 nm)/PbPc (20 nm)/C₇₀ (50 nm) near $Q = 9 \text{ nm}^{-1}$

deposition of the C₇₀ layer onto the PbPc film, strongly suggesting that the crystallinity of the PbPc layer was increased by the deposition of the C₇₀ layer, which was manifested from the comparison of the intensities of the peaks near $Q = 9 \text{ nm}^{-1}$ in the Figure 4.5b. In addition to that, the (220) oriented fcc C₇₀ phase increased at the expense of the reduced amount of the (111) oriented FCC phase in the C₇₀ layer. These results are consistent with the increase of the absorption intensity at a wavelength of 940 nm via the deposition of C₇₀. This kind of reconstruction of the organic molecules during Stranski-Krastanov growth in a heteroepitaxy system was also reported by Barrena et al.⁹⁷ The crystalline structure can be modified by the strain energy induced from lattice mismatch between substrate and overlayer in organic heteroepitaxy system because organic films are softer than inorganic films. These results can be summarized as follows: (1) CuBr acts as a templating layer to increase the crystallinity of PbPc layer, (2) the crystalline PbPc layer acts as a templating layer for C₇₀ molecules to form crystals with a preferred (220) orientation, and (3) the crystallinity of the PbPc bottom layer is increased by the deposition of the C₇₀ overlayer. The growth mode is schematically represented by the cartoon images in Figure 4.6.

4.3.4 Lattice modelling by energetic consideration

The templating effect can be explained by the model of quasi-epitaxial

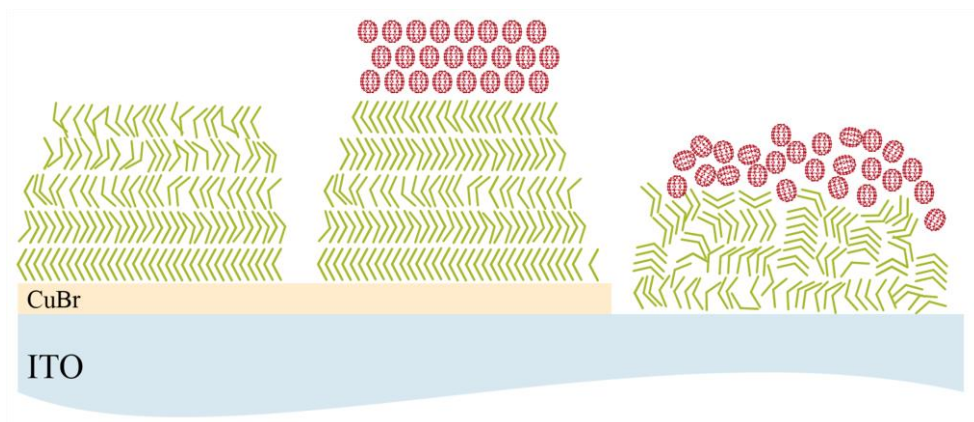


Figure 4.6 A cartoon image of multi-layer epitaxy film comprised of ITO/CuBr/PbPc, ITO/CuBr/PbPc/C₇₀ and ITO/PbPc/C₇₀.

Table 4.2 The lattice parameters of zinc blende CuBr, monoclinic PbPc and FCC C₇₀ are summarized.

	a [Å]	b [Å]	c [Å]	$\alpha = \beta = \gamma$ [°]
CuBr	5.695	5.695	5.695	90
PbPc monoclinic	25.48	25.48	3.73	90
C ₇₀ FCC	14.89	14.89	14.89	90

growth in organic films, where the dimensionless potential V/V_0 , representing the lattice matching between the substrate and the overlayer, is used as the parameter.⁸⁰ The value of V/V_0 is determined by the degree of commensurism between the overlayer and the substrate in the range $-0.5 \leq V/V_0 \leq 1$. $V/V_0 = 1$ for incommensurism, $V/V_0 = 0.5$ for coincidence, $V/V_0 = 0$ and $V/V_0 = -0.5$ for commensurism on nonhexagonal and hexagonal substrates, respectively. The lattice parameters of zinc blende CuBr, monoclinic PbPc and FCC C_{70} are summarized in Table 4.2.^{82,98,99} The potential V/V_0 's between the (111) plane of the CuBr crystal and the (320) plane of the monoclinic PbPc crystal, and between the (320) plane of the monoclinic PbPc crystal and the (220) plane of the FCC C_{70} crystal, were calculated against the azimuthal angle (θ) and displayed in Figure 4.7a. The angle θ was defined as the angle between the vectors \mathbf{a}_1 and \mathbf{b}_1 , with \mathbf{b}_1 and \mathbf{c}_1 defining the azimuthal angles between the overlayer and substrate in Figure 4.7b. The size of the overlayer was 55×55 . The results clearly show that the minimum potential between the (111) plane of the CuBr crystal and the (320) plane of the monoclinic PbPc crystal are derived at an angle of 20° . The minimum potential between the (320) plane of the monoclinic PbPc crystal and the (220) plane of the C_{70} crystal was obtained at an angle of 90° . The arrangement of CuBr, PbPc and C_{70} are schematically represented in Figure 4.7b, exhibiting the multilayer epitaxy.

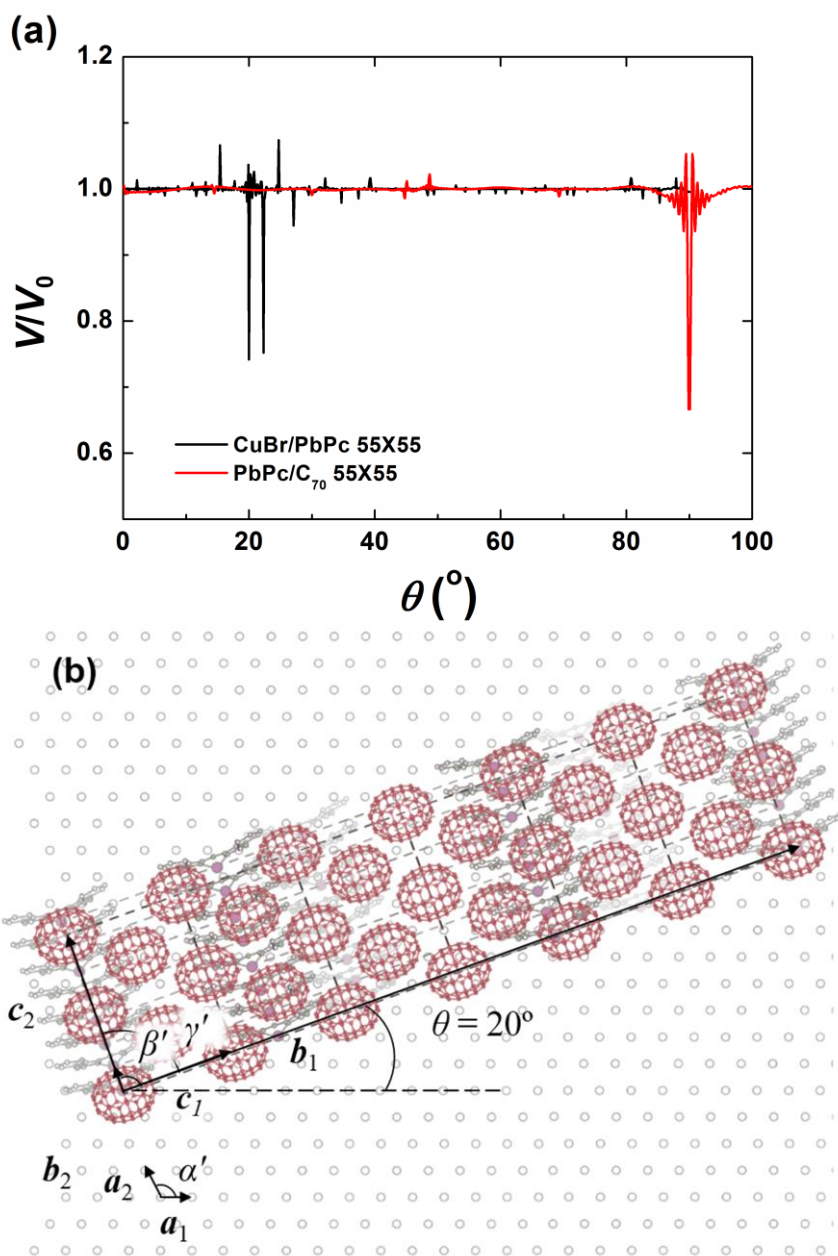


Figure 4.7 (a) The calculated dimensionless potential V/V_0 of CuBr (111)/PbPc monoclinic (320) and PbPc monoclinic (320)/C₇₀ FCC (220). (b) Schematic representation of PbPc monoclinic (320) and C₇₀ FCC (110) unit cells on zinc blende CuBr (111).

4.4 Conclusion

We demonstrated the multilayer epitaxy composed of ITO/CuBr/PbPc/C₇₀ and successfully fabricated OPVs with multilayer epitaxy films. The CuBr layer worked well as a templating layer to form the monoclinic PbPc molecules. In addition, the crystallized PbPc molecules act as a templating layer for the C₇₀ overlayer. As a result, the L_D values of the PbPc and C₇₀ layers were improved at the same time, from 5.6 nm to 8.8 nm for PbPc and from 6.9 nm to 13.8 nm for C₇₀. As a result, the OPV device with CuBr showed a 1.6 fold enhancement in the η_p , which resulted from the increase in the J_{SC} value. Furthermore, the results from the calculations of the dimensionless potential V/V_0 for the layers show that the templating effects of each layer can be explained by the quasi-epitaxial growth.

The increment of the exciton diffusion length in both donor and acceptor layers has been a major issue in increasing the short-circuit current in organic solar cells. The multilayer epitaxy demonstrated in this study not only explains the origin of the effect of the templating layer on the organic (donor) layer to control its crystal structure but also extends the concept of the epitaxy to the organic/organic multilayers to improve the light harvesting from the overlying organic (acceptor) layer. This multilayer epitaxy method can easily be extended to other sets of the materials with known lattice parameters of organic crystals and will generally contribute to

finding a proper combination of materials, for instance, to develop new templating materials and acceptor molecules for a given excellent donor material or vice versa to improve the performance of OPVs.

Chapter 5

Summary and conclusions

In this thesis, the use of templating materials for improving the optoelectronic properties of the organic layers are reported and the mechanism of the templating effects is discussed. Moreover, the efficient organic photovoltaics were successfully demonstrated with copper halogen compounds as templating layers.

Firstly, in chapter 2, we investigated the origin of low photo-stability of the OPV device with CuI templating layer. The OPV device with a CuI interfacial layer increases the efficiency significantly to 3.3%, it is 2.6 times higher value of the η_p compared to the device without CuI layer. However, the photo-stability is lowered even further. The TOF-SIMS analysis reveals that the diffusion of Cu atoms or ions was the origin of the photo-degradation of the device. In the contrary, the insertion of the MoO₃ layer between the ITO and CuI prevents the diffusion of Cu atoms or ions due to the formation of the CuMoO_x complexes under UV illumination. Resultantly, the device with a MoO₃/CuI double interfacial layer showed a much higher stability under illumination and did not show any degradation in the measured range.

In chapter 3, the origin of the templating effects on the growth of PbPc and the performance of OPVs were investigated by using three copper

halogen compounds (CuCl, CuBr, CuI) possessing different lattice parameters as the templating layers. The templating effects were able to be described by heteroepitaxial growth of organic molecules on the templating layers and the simple lattice modelling was used for the evaluation of the degree of epitaxy of the overlayer-substrate systems. The result from calculation of the dimensionless potential of each systems predicted that the PbPc monoclinic phase with the (320) orientation forms the coincidence epitaxy most favourably using CuI as the templating layer minimizing the potential energy due to the least lattice mismatch between the organic crystal and templating layer followed by CuBr and CuCl. The crystallinity of the PbPc films was the highest on CuI followed by CuBr and CuCl, resulting in the broadening of Q-band absorption in the same order. The results showed good correlation between the degree of epitaxy and the crystallinity of PbPc overlayers. Moreover, the growth mode of the PbPc films were influenced by the degree of the lattice mismatch between the organic crystal and templating layer. Large mismatch (PbPc on ITO) resulted in the island (VW) growth mode with low surface coverage but small mismatch (PbPc on CuI) resulted in the SK growth mode with much better surface coverage. Furthermore, the performance of OPVs was consistent with the prediction from the calculation results and the observation from the optical and structural analyses.

In chapter 4, the templating effect extends to multilayers to increase the crystallinity and to modify the orientation of the crystals of both PbPc and

C_{70} layers at the same time by adopting CuBr as a templating layer on ITO. The formation of a monoclinic phase with a preferred orientation of (320) for PbPc and a fcc phase with a preferred orientation of (220) for C_{70} on the PbPc layer is revealed by XRD patterns. As a result, the L_D values of the PbPc and C_{70} layers were improved at the same time, from 5.6 nm to 8.8 nm for PbPc and from 6.9 nm to 13.8 nm for C_{70} to enhance the η_p of the planar heterojunction OPVs composed of PbPc and C_{70} . Furthermore, the results from the calculations of the dimensionless potential V/V_0 for the layers show that the templating effects of each layer can be explained by the quasi-epitaxial growth.

Our results indicate that the selection of materials and the combination of interfacial layers for the templating layer are important to improve the efficiency and stability of the small molecular OPVs. Furthermore, we propose two conditions for efficient templating layer from our results. First, strong interaction between templating materials and organic molecules for active layer is essential. Ionic compounds would be promising candidate for the templating layer. After then, the lattice matching is important to achieve the high crystalline structure for whole layers.

In this thesis, we used simple analytic function for the evaluating the epitaxial growth. For the precise description and prediction of the epitaxial system, considering the molecular dynamics and exact potential of each atoms in molecules. However, our approach provide meaningful insight to predict the heteroepitaxial growth of molecules on the substrates and

understand the growth modes. Moreover, we successfully apply the multilayer heteroepitaxial system to OPV on the basis of the prediction.

We believe that the application of the concept of heteroepitaxy is not limited to our specific system but can be a general phenomenon in organic/organic and organic/inorganic multilayer systems and the degree of the heteroepitaxy depends on the interaction energy between the templating layer and the overlayer. This multilayer epitaxy method can easily be extended to other sets of the materials with known lattice parameters of organic crystals and will generally contribute to finding a proper combination of materials, for instance, to develop new templating materials and acceptor molecules for a given excellent donor material or vice versa to improve the performance of not only OPVs but also OTFTs.

Bibliography

1. C. W. Tang, *Appl. Phys. Lett.* 48, 183 (1986).
2. X. Che, X. Xiao, J. D. Zimmerman, D. Fan, S. R. Forrest, *Adv. Energy Mater.* DOI: 10.1002/aenm.201400568
3. P. Sullivan, T. S. Jones, A. J. Ferguson, S. Heutz, *Appl. Phys. Lett* 91, 233114 (2007).
4. J. Yang, D. Yan, *Chem. Soc. Rev.* 38, 2634 (2009).
5. B. Yu, L. Huang, H. Wang, D. Yan, *Adv. Mater.* 22, 1017 (2010).
6. T. Sakurai, T. Ohashi, H. Kitazume, M. Kubota, T. Suemasu, K. Akimoto, *Org. Electron.* 12, 966 (2011).
7. W. Zhao, J. P. Mudrick, Y. Zheng, W. T. Hammond, Y. Yang, J. Xue, *Org. Electron.* 13, 129 (2012).
8. S. S. Roy, D. J. Bindl, M. S. Arnold, *J. Phys. Chem. Lett.* 3, 873 (2012).
9. K. Xiao, W. Deng, J. K. Keum, M. Yoon, I. V. Vlassiouk, K. W. Clark, A.-P. Li, I. I. Kravchenko, G. Gu, E. A. Payzant, B. G. Sumpter, S. C. Smith, J. F. Browning, D. B. Geohegan, *J. Am. Chem. Soc.* 135, 3680 (2013).
10. Y. Zhou, T. Taima, T. Kuwabara, K. Takahashi, *Adv. Mater.* 25, 6069 (2013).

11. S. Kawata, Y.-J. Pu, C. Ohashi, K.-I. Nakayama, Z. Hong, J. Kido, *J. Mater. Chem. C* 2, 501 (2014).
12. C. H. Cheng, J. Wang, G. T. Du, S. H. Shi, Z. J. Du, Z. Q. Fan, J. M. Bian, M. S. Wang, *Appl. Phys. Lett.* 97, 083305 (2010).
13. H.-S. Shim, H. J. Kim, J. W. Kim, S.-Y. Kim, W.-I. Jeong, T.-M. Kim, J.-J. Kim, *J. Mater. Chem.* 22, 9077 (2012).
14. T.-M. Kim, J. W. Kim, H.-S. Shim, J.-J. Kim, *Appl. Phys. Lett.* 101, 113301 (2012).
15. B. P. Rand, D. Cheyns, K. Vasseur, N. C. Giebink, S. Mothy, Y. Yi, V. Coropceanu, D. Beljonne, J. Cornil, J.-L. Brédas, J. Genoe, *Adv. Funct. Mater.* 22, 2987 (2012).
16. H. J. Kim, H.-S. Shim, J. W. Kim, H. H. Lee, J.-J. Kim, *Appl. Phys. Lett.* 100, 263303 (2012).
17. Y. Zhou, T. Taima, T. Miyadera, T. Yamanari, M. Kitamura, K. Nakatsu, Y. Yoshida, *Nano Lett.* 12, 4146 (2012).
18. Y. Zhou, T. Taima, T. Miyadera, T. Yamanari, M. Kitamura, K. Nakatsu, Y. Yoshida, *Appl. Phys. Lett.* 100, 233302 (2012).
19. J. W. Kim, H. J. Kim, T.-M. Kim, T. G. Kim, J.-H. Lee, J. W. Kim, J.-J. Kim, *Curr. Appl. Phys.* 13, 7 (2013).
20. J. C. Bernede, L. Cattin, M. Makha, V. Jeux, P. Leriche, J. Roncali, V. Froger, M. Morsli, M. Addou, *Sol. Energy Mater. Sol. Cells* 110, 107 (2013).

21. K. Vasseur, K. Broch, A. L. Ayzner, B. P. Rand, D. Cheyns, C. Frank, F. Schreiber, M. F. Toney, L. Froyen, P. Heremans, *ACS Appl. Mater. Interfaces* 5, 8505 (2013).
22. W.-I. Jeong, Y. E. Lee, H.-S. Shim, T.-M. Kim, S.-Y. Kim, J.-J. Kim, *Adv. Funct. Mater.* 22, 3089 (2012).
23. Y. Zhou, T. Taima, Y. Shibata, T. Miyadera, T. Yamanari, Y. Yoshida, *Solar Energy Materials and Solar Cells* 95, 2861 (2011).
24. D. Placencia, W. N. Wang, R. C. Shallcross, K. W. Nebesny, M. Brumbach, N. R. Armstrong, *Adv. Funct. Mater.* 12, 1913 (2009).
25. J. W. Kim, H. J. Kim, H. H. Lee, T. Kim, J.-J. Kim, *Adv. Funct. Mater.* 21, 2067 (2011).
26. T. Kaji, M. Zhang, S. Nakao, K. Iketaki, K. Yokoyama, C. T. Tang, M. Hiramoto, *Adv. Mater.* 23, 3320 (2011).
27. S. Yoo, B. Domercq, B. Kippelen, *Appl. Phys. Lett.* 85, 5427 (2004).
28. L. C. Palilis, P. A. Lane, G. P. Kushto, B. Purushomatan, J. E. Anthony, Z. H. Kafafi, *Organic Electronics* 9, 747 (2008).
29. G. Wei, X. Xiao, S. Wang, J. D. Zimmerman, K. Sun, V. V. Diev, M. E. Thompson and S. R. Forrest, *Nano Lett.*, 11, 4261 (2011).
30. V. Steinmann, N. M. Kronenberg, M. R. Lenze, S. M. Graf, D. Hertel, K. Meerholz, H. Bürckstümmer, E. V. Tulyakova and F. Würthner, *Adv. Energy Mater.*, 1, 888 (2011).
31. Y.-H. Chen, L.-Y. Lin, C.-W. Lu, F. Lin, Z.-Y. Huang, H.-W. Lin, P.-

- H. Wang, Y.-H. Liu, K.-T. Wong, J. Wen, D. J. Miller, S. B. Darling, *J. Am. Chem. Soc.* 134, 13616 (2012).
32. M. Riede, C. Urich, J. Widmer, R. Timmreck, D. Wynands, G. Schwartz, W.-M. Gnehr, D. Hildebrandt, A. Weiss, J. Hwang, S. Sundarraj, P. Erk, M. Pfeiffer, K. Leo, *Adv. Funct. Mater.* 21, 3019 (2011).
 33. Y. He, G. Zhao, B. Peng and Y. Li, *Adv. Funct. Mater.* 20, 3383 (2010).
 34. Y. Sun, C. Cui, H. Wang and Y. Li, *Adv. Energy Mater.*, 1, 1058 (2011).
 35. S. B. Rim, R. F. Fink, J. C. Schoneboom, P. Erk and P. Peumans, *Appl. Phys. Lett.* 91, 173504 (2007).
 36. D. W. Pashley, *Advance. Phys.* 5, 173 (1956).
 37. S. R. Forrest, *Chem. Rev.* 97, 1793 (1997).
 38. D.-M. Smilgies, E. J. Kintzel, Jr, *Phys. Rev. B* 79, 235413 (2009).
 39. E. Lorenz, C. Keil, D. Schlettwein, *J. Porphyrins Phthalocyanines* 16, 977 (2012).
 40. A. Hoshino, S. Isoda, H. Kurata, T. Kobayashi, *J. Applied. Phys.*, 76, 4113 (1994).
 41. P. Fenter, P. E. Burrows, P. Elsenberger, S. R. Forrest, *J. Cryst. Growth*, 152, 65 (1995).
 42. D. O. Hayward, B. M. W. Trapnell, *Chemisorption*, Butterworths, London (1964).

43. J. E. Lennard-Jones, Proc. R. Soc. London A 106, 463 (1924).
44. R. Buckingham, J. Corner, Proc. R. Soc. London A 189, 118 (1946).
45. J. A. Last, D. E. Hooks, A. C. Hillier, M. D. Ward, J. Phys. Chem. B, 103, 6723 (1999).
46. H.-Y. Chen, J. Hou, S. Zhang, Y. Liang, G. Yang, Y. Yang, L. Yu, Y. Wu, G. Li, Nat. Photonics 3, 649 (2009).
47. Y. Liang, Z. Xu, J. Xia, S.-T. Tsai, Y. Wu, G. Li, C. Ray, L. Yu, Adv. Mater. 22, E135 (2010).
48. T.-Y. Chu, J. Lu, S. Beaupré, Y. Zhang, J.-R. Pouliot, S. Wakim, J. Zhou, M. Leclerc, Z. Li, J. Ding, Y. Tao, J. Am. Chem. Soc. 133, 4250 (2011).
49. H. Zhou, L. Yang, A. C. Stuart, S. C. Price, S. Liu, W. You, Angew. Chem. Int. Ed. 50, 2995 (2011).
50. Z. He, C. Zhong, X. Huang, W.-Y. Wong, H. Wu, L. Chen, S. Su, Y. Cao, Adv. Mater. 23, 4636 (2011).
51. L. Dou, J. You, J. Yang, C.-C. Chen, Y. He, S. Murase, T. Moriarty, K. Emery, G. Li, Y. Yang, Nat. Photonics 6, 180 (2012).
52. M. Hirade, C. Adachi, Appl. Phys. Lett. 99, 153302 (2011).
53. M. Zhang, H. Wang, H. Tian, Y. Geng, C. W. Tang, Adv. Mater. 23, 4960 (2011).
54. J. Zhou, X. Wan, Y. Liu, G. Long, F. Wang, Z. Li, Y. Zuo, C. Li, Y. Chen, Chem. Mater. 23, 4666 (2011).
55. L.-Y. Lin, Y.-H. Chen, Z.-Y. Huang, H.-W. Lin, S.-H. Chou, F. Lin, C.-

- W. Chen, Y.-H. Liu, K.-T. Wong, *J. Am. Chem. Soc.* 133, 15822 (2011).
56. M. Riede, C. Urich, J. Widmer, R. Timmreck, D. Wynands, G. Schwartz, W. -M. Gnehr, D. Hildebrandt, A. Weiss, J. Hwang, S. Sundarraj, P. Erk, M. Pfeiffer, K. Leo, *Adv. Funct. Mater.* 21, 3019 (2011).
 57. Y. Sun, G. C. Welch, W. L. Leong, C. J. Takacs, G. C. Bazan, A. J. Heeger, *Nat. Mat.* 11, 44 (2012).
 58. S.-W. Chiu, L.-Y. Lin, H.-W. Lin, Y.-H. Chen, Z.-Y. Huang, Y.-T. Lin, F. Lin, Y.-H. Liu, K.-T. Wong, *Chem. Commun.* 48, 1857 (2012).
 59. S. M. Schultes, P. Sullivan, S. Heutz, B. M. Sanderson, T. S. Jones, *Mater. Sci. Eng., C* 25, 858 (2005).
 60. Z. R. Hong, Z. H. Huang, X. T. Zeng, *Chem. Phys. Lett.* 425, 62 (2006).
 61. Z. R. Hong, B. Maennig, R. Lessmann, M. Pfeiffer, K. Leo, P. Simon, *Appl. Phys. Lett.* 90, 203505 (2007).
 62. L. Chen, Y. Tang, X. Fan, C. Zhang, Z. Chu, D. Wang, D. Zou, *Org. Electron.* 10, 724 (2009).
 63. S. Pfuetzner, J. Meiss, A. Petrich, M. Riede, K. Leo, *Appl. Phys. Lett.* 94, 253303 (2009).
 64. M. Hermenau, S. Scholz, Karl Leo, M. Riede, *Sol. Energy Mater. Sol. Cells*, 95, 1278 (2011).
 65. M. Hermenau, M. Riede, K. Leo, S. A. Gevorgyan, F. C. Krebs, K.

- Norrman, *Sol. Energy Mater. Sol. Cells* 95, 1268 (2011).
66. M. Rusu, J. Strotmann, M. Vogel, M. C. Lux-Steiner, K. Fostiropoulos, *Appl. Phys. Lett.* 90, 153511 (2007).
 67. R. Lessmann, Z. Hong, S. Scholz, B. Maennig, M. K. Riede, K. Leo, *Org. Electron.* 11, 539 (2010).
 68. S. Schäfer, A. Petersen, T. Wagner, R. Kniprath, D. Lingenfeller, A. Zen, T. Kirchartz, B. Zimmermann, U. Würfel, X. Feng, T. Mayer, *Phys. Rev. B* 83, 165311 (2011).
 69. Y. Kanai, T. Matsushima, H. Murata, *Thin Solid Films* 518, 537 (2009).
 70. A. Hancox, P. Sullivan, K. V. Chauhan, N. Beaumont, L. A. Rochford, R. A. Hatton, T. S. Jones, *Org. Electron.* 11, 2019 (2010).
 71. Y. Sun, C. J. Takacs, S. R. Cowan, J. H. Seo, X. Gong, A. Roy, A. J. Heeger, *Adv. Mater.* 23, 2226 (2011).
 72. J.-H. Lee, D.-S. Leem, J.-J. Kim, *Org. Electron.* 9, 805 (2008).
 73. T. Sakurai, R. Fukasawa, K. Saito, K. Akimoto, *Org. Electron.* 8, 702 (2007).
 74. K. Norrman, F. C. Krebs, *Sol. Energy Mater. Sol. Cells* 90, 213 (2006).
 75. K. Q. Ngo, P. Philipp, Y. Jin, S. E. Morris, M. Shtein, J. Kieffer, T. Wirtz, *Surf. Interface Anal.* 43, 194 (2011).
 76. K. Vasseur, B. P. Rand, D. Cheyns, L. Froyen, P. Heremans, *Chem. Mater.* 23, 886 (2011).
 77. W. Zhao, W.-L. Zhou, L.-Q. Chen, Y.-Z. Huang, Z.-B. Zhang, K. K.

- Fung, Z.-X. Zhao, *J. Solid State Chem.* 112, 412 (1994).
78. A. Koma, *Prog. Crystal Growth and Charact.* 30, 129 (1995).
 79. S. R. Forrest and P. E. Burrows, *Supramol. Sci.* 4, 127 (1997).
 80. D. E. Hooks, T. Fritz, M. D. Ward, *Adv. Mater.* 13, 227 (2001).
 81. S. Kono, T. Ishii, T. Sagawa, T. Kobayasi, *Phys. Rev. B: Solid State* 8, 795 (1973).
 82. S. Hull, D. A. Keen, *Phys. Rev. B: Condens. Matter Mater. Phys.* 50, 5868 (1994).
 83. A. Miyamoto, K. Nichogi, A. Taomoto, T. Nambu, M. Murakami, *Thin Solid Films* 256, 644 (1995).
 84. L. Ottaviano, L. Lozzi, A. R. Phani, A. Ciattoni, S. Santucci, S. Di Nardo, *Appl. Surf. Sci.* 136, 81 (1998).
 85. K. Mizoguchi, K. Mizui, D. G. Kim, M. Nakayama, *Jpn. J. Appl. Phys.* 41, 6421 (2002).
 86. S. Tabuchi, H. Tabata, T. Kawai, *Surf. Sci.* 571, 117 (2004).
 87. I. Daruka and A.-L. Barabási, *Phys. Rev. Lett.* 79, 3708 (1997).
 88. Z. Li, G. He, X. Wan, Y. Liu, J. Zhou, G. Long, Y. Zuo, M. Zhang, Y. Chen, *Adv. Energy Mater.* 2, 74 (2012).
 89. J. Huang, C. Zhan, X. Zhang, Y. Zhao, Z. Lu, H. Jia, B. Jiang, J. Ye, S. Zhang, A. Tang, Y. Liu, Q. Pei, J. Yao, *ACS Appl. Mater. Interfaces* 5, 2033 (2013).
 90. A. K. K. Kyaw, D. H. Wang, D. Wynands, J. Zhang, T.-Q. Nguyen, G. C. Bazan, A. J. Heeger, *Nano Lett.* 13, 3796 (2013).

91. G. Chen, H. Sasabe, Z. Wang, X.-F. Wang, Z. Hong, Y. Yang, J. Kido, *Adv. Mater.* 24, 2768 (2012).
92. R. Fitzner, E. Mena-Osteritz, A. Mishra, G. Schulz, E. Reinold, M. Weil, C. Körner, H. Ziehlke, C. Elschner, K. Leo, M. Riede, M. Pfeiffer, C. Urich, P. Bäuerle, *J. Am. Chem. Soc.* 134, 11064 (2012).
93. X. Xiao, K. J. Bergemann, J. D. Zimmerman, K. Lee, S. R. Forrest, *Adv. Energy Mater.* 4, 1301557, (2013).
94. W. J. Potscavage, Jr., A. Sharma, B. Kippelen, *Acc. Chem. Res.* 42, 1758 (2009).
95. W. Chen, D.-C. Qi, H. Huang, X. Gao, T. S. Wee, *Adv. Funct. Mater.* 21, 410 (2011).
96. J. Lee, S.-Y. Kim, C. Kim, J.-J. Kim, J.-J., *Appl. Phys. Lett.* 97, 083306 (2010).
97. E. Barrena, D. G. de Oteyza, S. Sellner, D. Helmut, *Phys. Rev. Lett.* 97, 076102 (2006).
98. K. Ueki, *Acta Crystallogr. Sect. B: Struct. Crystallogr. Cryst. Chem.* 29, 2290 (1973).
99. M. C. Valsakumar, N. Subramanian, M. Yousuf, P. Ch. Sahu, Y. Hariharan, A. Bharathi, V. Sankara Sastry, J. Janaki, G. V. N. Rao, T. S. Radhakrishnan, C. S. Sundar, *Phys. Rev. B* 48, 9080 (1993).

초 록

유기태양전지는 대면적, 유연 기판으로 생산이 가능하고 저가 공정이며 환경친화적이라는 점에서 최근 많은 연구가 이루어지고 있다. 하지만, 유기태양전지는 아직 무기물 기반 태양전지에 비하여 상대적으로 낮은 에너지변환효율을 보이고 있으며, 낮은 안정성 또한 발전에 사용하기에 걸림돌이 되고 있는 실정이다. 따라서, 유기태양전지의 양산을 위해서 에너지변환효율과 안정성을 함께 증대시키는 것이 중요한 연구주제이다. 본 학위 논문에서는 템플릿 물질을 이용하여 유기물 층의 전기-광학적 성질을 향상시킨 결과와 그 기작에 대한 연구 결과에 대해 논의하였다.

먼저, zinc phthalocyanine (ZnPc) 기반 유기태양전지의 에너지변환효율과 광안정성을 molybdenum oxide (MoO_3)와 copper iodide (CuI)로 이루어진 이중층을 사용하여 향상시켰다. ZnPc 박막의 흡수가 CuI를 템플릿층으로 사용하였을 때 1.6배 증가하였고, 결과적으로 유기태양전지의 에너지변환효율이 2.6배 증가하였다. 하지만 CuI를 사용하였을 때 유기태양전지의 광안정성이 사용하지 않았을 때에 비하여 더 낮아지는 현상이

나타났다. 이를 분석하기 위하여 time-of-flight secondary ion mass spectrometry (TOF-SIMS)를 이용하였고, Cu 원자 또는 이온이 광활성층으로 확산되는 현상으로 인하여 빛에 의해 소자 효율이 감소한다는 것을 밝혔다. Cu 원자 또는 이온의 확산을 막기 위하여 MoO₃를 indium tin oxide (ITO)와 CuI 사이에 삽입하였고, 소자의 광안정성을 효과적으로 향상시켰다.

이와 같은 템플릿 효과의 기작에 대해 연구하기 위하여, lead-phthalocyanine (PbPc)를 전자수용체로 사용하고 서로 다른 격자 상수를 갖는 구리화합물 (CuCl, CuBr, CuI)를 템플릿 층으로 사용하여 PbPc 박막의 전기-광학적 성질과 태양전지 특성에 대하여 분석하였다. PbPc 박막의 결정도가 격자상수가 커지는 순서인 CuCl, CuBr 그리고 CuI 순으로 증가하였고, PbPc 박막의 Q-밴드 흡수 또한 같은 순서로 증가하였다. 이와 같은 템플릿 효과를 이해하기 위하여 이중에피택시 성장 이론을 도입하였고, 상지층-기판 구조에서 격자모형을 고려한 에너지를 계산하였다. 또한, 유기태양전지의 효율의 변화가 계산 및 관측 결과와 일치하였다.

최종적으로, 템플릿 효과를 다중층으로 확대하여 PbPc 층뿐만 아니라 C₇₀ 층의 결정도를 동시에 증가시킨 결과를 얻을 수 있었다. X-선을 이용하여 분석한 결과, PbPc 분자는 CuBr 위에서

monoclinic (320)으로 성장하고, C₇₀분자는 monoclinic (320) PbPc 박막 위에서 fcc (110) 면으로 성장하였다. 다중층 에피택시 성장으로 PbPc와 C₇₀의 엑시톤 이동거리가 각각 5.6과 6.9 nm에서 8.8과 13.8 nm로 증가하였고, 유기태양전지 소자의 효율 또한 1.6배 증가하였다. 이와 같은 결과는 앞에서와 마찬가지로 이중에피택시 성장이론을 도입하여 이해할 수 있었다.

주요어: 유기태양전지, 저분자, 진공증착공정, 결정성장, 유기에피택시, 광안정성

학 번: 2011 - 30784

CURRICULUM VITAE

Kim Tae-Min

Department of Materials Science and Engineering

Seoul National University, Seoul, 151-744, Korea

+82-2-875-2412 (Office), +82-2-889-8702 (Fax)

E-mail: clareo13@snu.ac.kr

Education

2011.3 ~ 2015.2 **PH.D.** in Materials Science and Engineering

Supervisor: Professor Jang-Joo Kim

Seoul National University, Seoul, Korea

2009.3 ~ 2011.2 **M.S.** in Materials Science and Engineering

Seoul National University, Seoul, Korea

2004.3 ~ 2009.2 **B.S.** in Materials Science and Engineering

Seoul National University, Seoul, Korea

Teaching Experiences

2013.1 ~ 2014.9 Teaching Fellow (TF), “Experiments in Materials

1”, #445.303

In Seoul National University, Seoul, Korea

Research Interests

- Fabrication of polymer solar cells and organic small molecule solar cells
- Origin of photo-degradation in small molecular solar cells
- Control of molecular orientation for small molecular organic solar cells
- Organic molecular epitaxy
- Organic electronics (OLEDs, OTFTs)

Professional Skills

- Design and fabrication of organic electronic devices: thermal evaporator, sputtering system, glove-box, spin coater
- The optoelectronic analyses on organic semiconductor: UV-vis-NIR absorption spectroscopy, interpretation of current density-voltage characteristics and incident photon-to-current efficiency, time-of-flight, impedance spectroscopy
- The structural characterization of organic films: atomic force microscopy, alpha-step, x-ray spectroscopy

Scholarship and Fellowship

- Brain Korea 21 Scholarship (2009.3 ~)
- WCU(World Class University) project through National Research

Foundation of Korea funded by the Ministry of Education, Science and Technology (2011.3 ~)

- Hi Seoul Science Fellowship funded by Seoul Scholarship Foundation (2011.9 ~ 2013.2)

Awards

- **Tae-Min Kim**, Ji Whan Kim, Hyun Sub Shim and Jang-Joo Kim, “Best Poster Award”, The 3rd Asian Conference on Organic Electronics, Nov. 4-6, 2011
- Ji Whan Kim, Hyo Jung Kim, **Tae-Min Kim**, Tae Gun Kim, Jeong-Hwan Lee, Jeong Won Kim and Jang-Joo Kim, “Best Poster Award”, The 3rd Asian Conference on Organic Electronics, Nov. 4-6, 2011

List of Publications

1. Beom-Soo Kim, **Tae-Min Kim**, Min-Soo Choi, Hyun-Sub Shim and Jang-Joo Kim, "Fully vacuum-processed perovskite solar cells with high open circuit voltage using MoO₃/NPB as hole extraction layers", *Organic Electronics*, 2015, 17, 102.
2. Jongchul Kwon †, **Tae-Min Kim** †, Hong-Se Oh, Jang-Joo Kim and Jong-In Hong, "Vacuum processable donor material based on dithieno[3,2-*b*:2',3'-*d*]thiophene and pyrene for efficient organic solar cells", *RSC Advances*, 2014, 4, 24453.
3. **Tae-Min Kim**, Hyo Jung Kim, Hyun-Sub Shim, Min-Soo Choi, Ji Whan Kim and Jang-Joo Kim, "Epitaxial growth of lead-phthalocyanine on copper halogen compounds as the origin of templating effects", *Journal of Materials Chemistry A*, 2014, 2, 8730.
4. **Tae-Min Kim**, Hyun-Sub Shim, Min-Soo Choi, Hyo Jung Kim, and Jang-Joo Kim, "Multilayer Epitaxial Growth of Lead Phthalocyanine and C70 Using CuBr as a Templating Layer for Enhancing the Efficiency of Organic Photovoltaic Cells", *ACS Applied Materials & Interfaces*, 2014, 6, 4286.
5. Sunghoon Jung, Sunghun Lee, Myungkwan Song, Do-Geun Kim, Dae Sung You, Jong-Kuk Kim, Chang Su Kim, **Tae-Min Kim**, Kwon-Hyeon Kim, Jang-Joo Kim, Jae-Wook Kang, "Extremely Flexible

- Transparent Conducting Electrodes for Organic Devices", *Advanced Energy Materials*, 4, 1300474, 2014
6. Jun Choi, Woosung Lee, Jin Woong Namgoong, **Tae-Min Kim**, Jae Pil Kim, "Synthesis and characterization of novel triazatetrabenzcorrole dyes for LCD color filter and black matrix", *Dyes and Pigments*, 99, 2, 2013
 7. Hyun-Sub Shim, Sei-Yong Kim, Ji Whan Kim, **Tae-Min Kim**, Chang-Heon Lee, Jang-Joo Kim, "An efficient interconnection unit composed of electron-transporting layer/metal/p-doped hole-transporting layer for tandem organic photovoltaics", *Applied Physics Letter*, 102, 203903 (2013)
 8. Ji Whan Kim, Hyo Jung Kim, **Tae-Min Kim**, Tae Gun Kim, Jeong-Hwan Lee, Jeong Won Kim and Jang-Joo Kim, "High performance Organic Planar Heterojunction Solar cells by controlling the Molecular orientation" *Current Applied Physics* 13 (2013) 7-11
 9. Dae-Ho Kim, **Tae-Min Kim**, Won-Ik Jeong, and Jang-Joo Kim, "Rhenium oxide as an efficient p-dopant to overcome S-shaped current density-voltage curves in organic photovoltaics with a deep highest occupied molecular orbital level donor layer", *Appl. Phys. Lett.* 101, 153303 (2012)
 10. **Tae-Min Kim** †, Ji Whan Kim †, Hyun-Sub Shim and Jang-Joo Kim,

- "High efficiency and high photo-stability zinc-phthalocyanine based planar heterojunction solar cells with a double interfacial layer" Applied Physics Letter, 101, 113301 (2012)
11. Jongchul Kwon, Jung-Pyo Hong, Seunguk Noh, **Tae-Min Kim**, Jang-Joo Kim, Changhee Lee, Seonghoon Lee and Jong-In Hong, "Pyrene end-capped oligothiophene derivatives for transistors and organic solar cells" New Journal of Chemistry 2012, 36, 1813-1818
 12. Won-Ik Jeong, Yang Eun Lee, Hyun-Sub Shim, **Tae-Min Kim**, Sei-Yong Kim and Jang-Joo Kim, "Photoconductivity of C60 as an Origin of Bias-Dependent Photocurrent in Organic Photovoltaics" Advanced Functional Materials 22, 14, 3089-3094, 2012
 13. Hyun-Sub Shim, Hyo Jung Kim, Ji Whan Kim, Sei-Yong Kim, Won-Ik Jeong, **Tae-Min Kim** and Jang-Joo Kim, "Enhancement of near-infrared absorption with high fill factor in lead phthalocyanine-based organic solar cells" Journal of Materials Chemistry, 22, 9077, 2012
 14. Hyo Jung Kim, Ji Whan Kim, Hyun Hwi Lee, **Tae-Min Kim**, Junhyuk Jang, Jang-Joo Kim, "Grazing Incidence Small-Angle X-ray Scattering Analysis of Initial Growth of Planar Organic Molecules Affected by Substrate Surface Energy", Journal of Physical Chemistry Letters, 2, 1710-1714 (2011)
 15. Ji Whan Kim, Hyo Jung Kim, Hyun Hwi Lee, **Taemin Kim**, and Jang-

Joo Kim, "Formation of bulk heterojunctions by alternative thermal deposition and its structure analysis for high efficiency small molecular organic photovoltaics", *Advanced Functional Materials*, 21, 2067 (2011)

List of Presentations

International Conference

1. **Tae-Min Kim**, Hyun-Sub Shim, Min-Soo Choi, Hyo Jung Kim and Jang-Joo Kim, "Multilayer Epitaxial Growth of Lead Phthalocyanine and C70 Using CuBr as a Templating Layer for Enhancing the Efficiency of Organic Photovoltaic Cells", 2014 Joint Symposium of Korean Society fo Photoscience - Korea Organic Solar Cell Society, Jun 20-21, 2014, Korea
2. **Tae-Min Kim**, Hyun-Sub Shim, Min-Soo Choi, and Jang-Joo Kim, "Multi-layer epitaxial growth of lead-phthalocyanine and C70 using CuBr as a templating layer for the efficiency enhancement of organic photovoltaic", 5th Asian Conference on Organic Electronics (A-COE 2013), November 13-15 (November 15), 2013, Korea
3. **Tae-Min Kim**, Hyun-Sub Shim, Min-Soo Choi, and Jang-Joo Kim, "Heteroepitaxial growth of lead-phthalocyanine and C70 using CuBr as a templating layer for the efficieny enhancement of organic photovoltaic

- cells", IRTG 2013 (8th German-Korean Polymer Symposium), August 26-29 (August 28), 2013, Germany
4. Hyun-Sub Shim, Sei-Yong Kim, Ji Whan Kim, **Tae-Min Kim**, Chang-Heon Lee, and Jang-Joo Kim, "An efficient interconnection unit composed of electron-transporting layer/metal/p-doped hole transporting layer for tandem organic photovoltaics", IRTG 2013 (8th German-Korean Polymer Symposium), August 26-29 (August 28), 2013, Germany
 5. Dae-Ho Kim, **Tae-Min Kim** and Jang-Joo Kim, "Rhenium oxide as an efficient p-dopant to overcome S-shaped current density-voltage curves in organic photovoltaics with a deep highest occupied molecular orbital level donor layer", SPIE Optics+Photonics 2013, 25-29 August (27 August), 2013, USA
 6. Won-Ik Jeong, Yang-Eun Lee, Hyun-sub Shim, **Tae-Min Kim**, Sei-Yong Kim, Jang-Joo Kim, "Photoconductivity of C60 as an Origin of Bias-Dependent Photocurrent in Organic Photovoltaics", IRTG 2013, 2013.02.27(2013.02.25-28)
 7. Dae-Ho Kim, **Tae-Min Kim**, Won-Ik Jeong, Jang-Joo Kim, "Rhenium oxide as an efficient p-dopant to overcome S-shaped current density-voltage curves in OPVs with a deep HOMO level donor layer", ACOE 2012, 2012.12.20 (2012.12.19-21), Japan

8. Dae-Ho Kim, **Tae-Min Kim**, Won-Ik Jeong, Jang-Joo Kim, "Rhenium oxide as an efficient p-dopant to overcome S-shaped current density-voltage curves in OPVs with a deep HOMO level donor layer", GOPVC 2012, 2012.11.19(2012.11.19-21)
9. Hyun-Sub Shim, Hyo Jung Kim, Ji Whan Kim, Sei-Yong Kim, Won-Ik Jeong, **Tae-Min Kim** and Jang-Joo Kim, "Near-infrared absorbing small molecular organic solar cells", The 8th TU-UT-SNU-TJU Student Workshop, 2012.10.17(2012.10.17-20)
10. **Tae-Min Kim**, Ji Whan Kim, Hyun Sub Shim, Jang-Joo Kim, "High efficiency and high photo-stability zinc-phthalocyanine based planar heterojunction solar cells with a double interfacial layer", ILCC 2012, 2012.08.20(2012.08.19~24)
11. **Tae-Min Kim**, Ji Whan Kim, Hyun Sub Shim, Jang-Joo Kim, "High efficiency and high photo-stability zinc-phthalocyanine based planar heterojunction solar cells with a double interfacial layer", 2nd ENGE 2012, Sep. 17, 2012
12. Dae-Ho Kim, **Tae-Min Kim**, Won-Ik Jeong, and Jang-Joo kim, "Efficient organic solar cells with high fill factor using rhenium oxide-doped hole transporting layer", IMID2012, Aug.28, 2012
13. Hyun-Sub Shim, Hyo Jung Kim, Ji Whan Kim, Sei-Yong Kim, Won-Ik Jeong, **Tae-Min Kim** and Jang-Joo Kim, "Enhancement of Near-

- Infrared absorption with high fill factor in lead phthalocyanine based organic solar cells", IMID2012, Aug. 28, 2012
14. Hyun-Sub Shim, Jang-Joo Kim, Hyo Jung Kim, Ji Whan Kim, Sei-Yong Kim, Won-Ik Jeong, **Tae-Min Kim**, "Enhanced sensitivity to near-infrared with high fill factor in small molecular organic solar cells", SPIE2012, Aug. 12 2012
 15. **Tae-Min Kim**, Ji Whan Kim, Hyun-Sub Shim and Jang-Joo Kim, "High Efficiency and high photo-stability zinc-phthalocyanine based planar heterojunction solar cells with a double interfacial layer", MRS 2012, Apr. 12, 2012
 16. **Tae-Min Kim**, Ji Whan Kim, Hyun Sub Shim and Jang-Joo Kim, "High efficiency and high photo-stability zinc-phthalocyanine based planar heterojunction solar cells with a double interfacial layer", The 3rd Asian Conference on Organic Electronics, Nov. 4-6 2011
 17. Ji Whan Kim, Hyo Jung Kim, **Tae-Min Kim**, Tae Gun Kim, Jeong-Hwan Lee, Jeong Won Kim and Jang-Joo Kim, "Enhanced performance of organic planar heterojunction solar cell by controlling the molecular orientation", The 3rd Asian Conference on Organic Electronics, Nov. 4-6 2011
 18. Ji Whan Kim, Hyo Jung Kim, **Tae-Min Kim**, Hyun Hwi Lee and Jang-Joo Kim, "Small molecular bulk heterojunction solar cells using

- alternative thermal deposition”, The 11th International Meeting on Information Display, 2011, Oct. 11-15, Seoul, Korea
19. **Tae-Min Kim**, Won-Ik Jeong and Jang-Joo Kim, “Wavelength dependent photo-degradation of organic planar heterojunction solar cells”, The 11th International Meeting on Information Display, 2011, Oct. 11-15, Seoul, Korea
 20. Hyo Jung Kim, Ji Whan Kim, **Tae-Min Kim**, Junghyuk Jang, Hyun Hwi Lee, “Controlling of initial molecular arrangement of copper(II) phthalocyanine for interpenetrating networks in a mixed donor/acceptor layer”, 2011 SPIE Optics+Photonics, Aug. 21-23, 2011
 21. Won-Ik Jeong, **Tae-Min Kim**, Jang-Joo Kim, “Bias dependent photocurrent originated from the photoconductivity of C60 in organic photovoltaics”, 3rd Hybrid and Organic Photovoltaics Conference, May 15-18, 2011
 22. **Tae-Min Kim**, Won-Ik Jeong, Jang-Joo Kim, “Efficient charge extraction for high photo-stability of organic planar heterojunction solar cells”, 3rd Hybrid and Organic Photovoltaics Conference, May 15-18, 2011
 23. Ji Whan Kim, Hyo Jung Kim, Hyun Hwi Lee, **Taemin Kim**, and Jang-Joo Kim, “Formation of small molecular bulk heterojunctions by alternative thermal deposition”, The 22nd International Conference on

Molecular Electronics and Devices, May 19-20, 2011, Pohang (Korea)

24. Ji Whan Kim, Hyo Jung Kim, Hyun Hwi Lee, **Taemin Kim**, Jang-Joo Kim, "Alternative thermal deposition for high efficiency small molecular organic photovoltaics", The Asian Conference on Organic Electronics 2010 & The Asian Symposium on Organic Materials for Electronics and Photonics 2010, Nov. 3-5, 2010
25. **Tae-Min Kim**, Won-Ik Jeong, Jang-Joo Kim, "Influence of photo-degradation on the properties of the metalphthalocyanine based small molecule organic photovoltaic cells", The Asian Conference on Organic Electronics 2010 & The Asian Symposium on Organic Materials for Electronics and Photonics 2010, Nov. 3-5, 2010

Domestic Conference

1. Won-Ik Jeong, Yang Eun Lee, Hyun-Sub Shim, **Tae-Min Kim**, Sei-Yong Kim and Jang-Joo Kim, "Photoconductivity of C60 as an origin of bias-dependent photocurrent in organic photovoltaics", 한국 유기태양 전지학회 2012 하계 심포지엄, June 27, 2012
2. **Tae-Min Kim**, Ji Whan Kim, Hyun-Sub Shim and Jang-Joo Kim, "High efficiency and high photo-stability zinc-phthalocyanine based planar heterojunction solar cells with a double interfacial layer", 한국 유기태

양전지학회 2012 하계 심포지엄, June 27, 2012

3. Won-Ik Jeong, Yang Eun Lee, Hyun-Sub Shim, **Tae-Min Kim**, Sei-Yong Kim, Jang-Joo Kim, “Photoconductivity of C60 as an origin of bias dependent photocurrent in organic photovoltaics”, 제17회 유기태양전지 심포지엄, Dec. 15-16, 2011
4. **김태민**, 정원익, 김장주, “Wavelength dependent photo-degradation of organic planar heterojunction solar cells”, 2011 한국태양광학술대회 및 제 6회 한중일 태양광발전 국제공동 심포지엄, Sep. 28-30, 2011
5. 김효정, 김지환, **김태민**, 김장주, “The molecular arrangement of M-Pcs (metal phthalocyanine) and the formation of bulkheterojunction structure in a mixed donor/acceptor layer”, 2011 한국태양광학술대회 및 제 6회 한중일 태양광발전 국제공동 심포지엄, Sep. 28-30, 2011
6. 정원익, **김태민**, 심현섭, 이양은, 김세용, 김장주, “Bias dependent photocurrent originated from the photoconductivity of C60 in organic photovoltaics”, 2011 한국태양광학술대회 및 제 6회 한중일 태양광발전 국제공동 심포지엄, Sep. 28-30, 2011
7. 심현섭, **김태민**, 김장주, “The effect of buffer layer in small molecular

- near-infrared photodetector”, 2011 한국고분자학회 춘계 학술대회,
April 7-8, 2011
8. 김태민, 정원익, 김장주, “Enhance the photo-stability of copper phthalocyanine/fullerene based small molecular photovoltaic cells by insertion of buffer layer”, 2011 한국고분자학회 춘계 학술대회,
April 7-8, 2011
9. 김지환, 김태민, 이현휘, 김장주, 김효정, “The role of CuI layer on the molecular arrangement of copper(II) phthalocyanine in a mixed donor/acceptor layer”, 2011 한국고분자학회 춘계 학술대회, April 7-8, 2011
10. 정원익, 김태민, 김세용, 김장주, “Wavelength and dc-bias dependent photocurrent collection of the organic planar heterojunction solar cells”, 2011 한국고분자학회 춘계 학술대회, April 7-8, 2011

List of Patents

1. 홍종인, 김장주, 권종철, **김태민**, “싸이오펜 유도체 화합물, 이의 제조방법 및 이를 이용한 유기 태양전지”, 10-2013-0018834 (2013.02.21)
2. 홍종인, 김장주, 전용준, **김태민**, “벤조싸이아다디아졸 유도체 화합물, 이의 제조방법 및 이를 이용한 유기 태양전지”, 10-2013-0018835 (2013.02.21)
3. 김대호, **김태민**, 정원익, 김장주, “Rhenium oxide as an efficient p-dopant to overcome S-shaped J-V curves in organic photovoltaics with a deep HOMO level donor layer”, KD-42530-PCT, (2012.04.22)
4. 김대호, **김태민**, 정원익, 김장주, “낮은 최고준위점유분자궤도 에너지 준위의 전자 공여체를 사용한 유기 태양전지에서 “S”형태의 전류-전압 그래프를 극복하기 위한 효과적인 p형 도펀트, 레늄 산화물”, 10-2012-0116068 (2012.11.14), 등록번호 1014198090000 (2014.07.09)
5. 김장주, **김태민**, 김지환, "이중 계면층을 포함한 저분자 유기태양 전지", 출원번호 10-2012-0055529 (2012.05.24), 등록번호 1013716090000 (2014.07.04)
6. 김장주, **김태민**, 김지환, " Low molecular organic solar cell

comprising double interfacial layer", PCT/KR2012/006690, (2013.11.28)